ACS NANO

Open Access

www.acsnano.org

ARTICLE

Hydrogel Loaded with Aminoethyl Anisamide-Modified Exosomes Attenuates Hepatic Fibrosis by Targeting Activated Hepatic Stellate Cells

Zongbin Sun, Qiuxia Zheng, Yue Zhang, Chongyang Bai, Fanghong Wang, Ping Yang, Dan Zhu, Xiaoyuan Liu, Shang Li, Desheng Liu, Rui Li, Liu He, Jia Yao,* and Xun Li*

Cite This: *ACS Nano* 2025, 19, 34575−34595

Read Online

ACCESS | Metrics & More | Article Recommendations | Supporting Information

ABSTRACT: **Stem cell-based regenerative research has highlighted the therapeutic potential of human umbilical cord mesenchymal stem cell-derived exosomes (hucMSC-Exos) for hepatic tissue regeneration and repair. However, exosomes undergo rapid clearance following systemic administration, limiting their therapeutic potential because of insufficient retention and sustained release. In this study, an innovative hydrogel-mediated delivery platform encapsulating aminoethyl anisamide (AEAA)-functionalized exosomes was developed to mitigate hepatic fibrosis. By synthesizing a hydrogel (CMC-OD/TA-Fe(III), Gel) composed of carboxymethyl chitosan, oxidized dextran, and iron tannate, and then encapsulating umbilical cord mesenchymal stem cell-derived exosomes functionalized by AEAA (AEAA-Exos), we implanted this Gel/AEAA-Exos into mice with hepatic fibrosis by intraperitoneal injection to evaluate the therapeutic effect of the hydrogel. The hydrogel had favorable physical properties, optimal biocompatibility, and a sustained-release profile. And Gel/AEAA-Exos system significantly reduced oxidative stress and alleviated hepatic fibrosis. Additionally, RNA-seq revealed that the Gel/AEAA-Exos system ameliorates hepatic fibrogenesis mainly by modulating oxidative stress, collagen deposition, and inflammatory cascade in liver tissues. This strategy offers a targeted and efficient approach for treating liver fibrosis induced by chronic hepatic injury and improves targeting efficiency and therapeutic outcomes through engineered exosome delivery.**

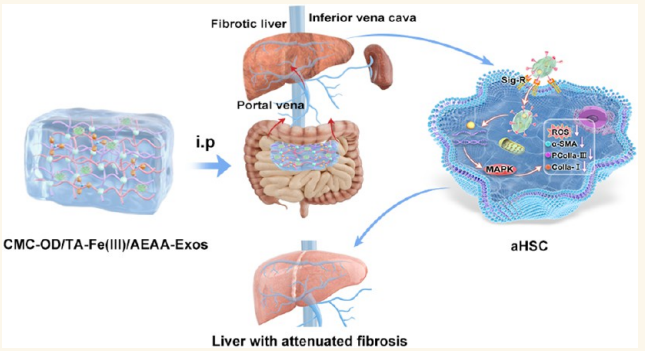

KEYWORDS: *hydrogel, AEAA-engineered exosomes, sustained release, target, antihepatic fibrosis*

1. INTRODUCTION

Progressive hepatic fibrogenesis is a hallmark pathological response to persistent liver lesions, is fundamentally driven by dysregulated deposition of extracellular matrix (ECM) components, and is a dynamic process involving progressive tissue remodeling.[1,2] Excessive fibrotic progression leads to substantial scar tissue formation, resulting in architectural distortion of the hepatic lobules and progressive hepatic dysfunction, ultimately culminating in cirrhosis and hepatic failure.[3] Cirrhosis caused by the development of hepatic fibrosis is the strongest factor in the occurrence of hepatocellular carcinoma.[4] Global mortality statistics document approximately 2 million annual deaths from hepatobiliary disorders, with cirrhotic liver failure accounting for half of these fatalities (1 million cases), positioning it as the 11th leading cause of worldwide mortality.[5] Therefore, treatment and prevention of chronic hepatic fibrosis are urgent issues to be solved. The occurrence of hepatic fibrosis is significantly associated with lesion-induced oxidative stress, which activates hepatic stellate cells (HSCs) to secrete matrix proteins.[6] Thus, HSCs may be key target for hepatic fibrosis treatment, and reducing the effects of oxidative stress on HSCs represents a new strategy for hepatic fibrosis therapy.

Received: April 9, 2025
Revised: September 11, 2025
Accepted: September 12, 2025
Published: September 23, 2025

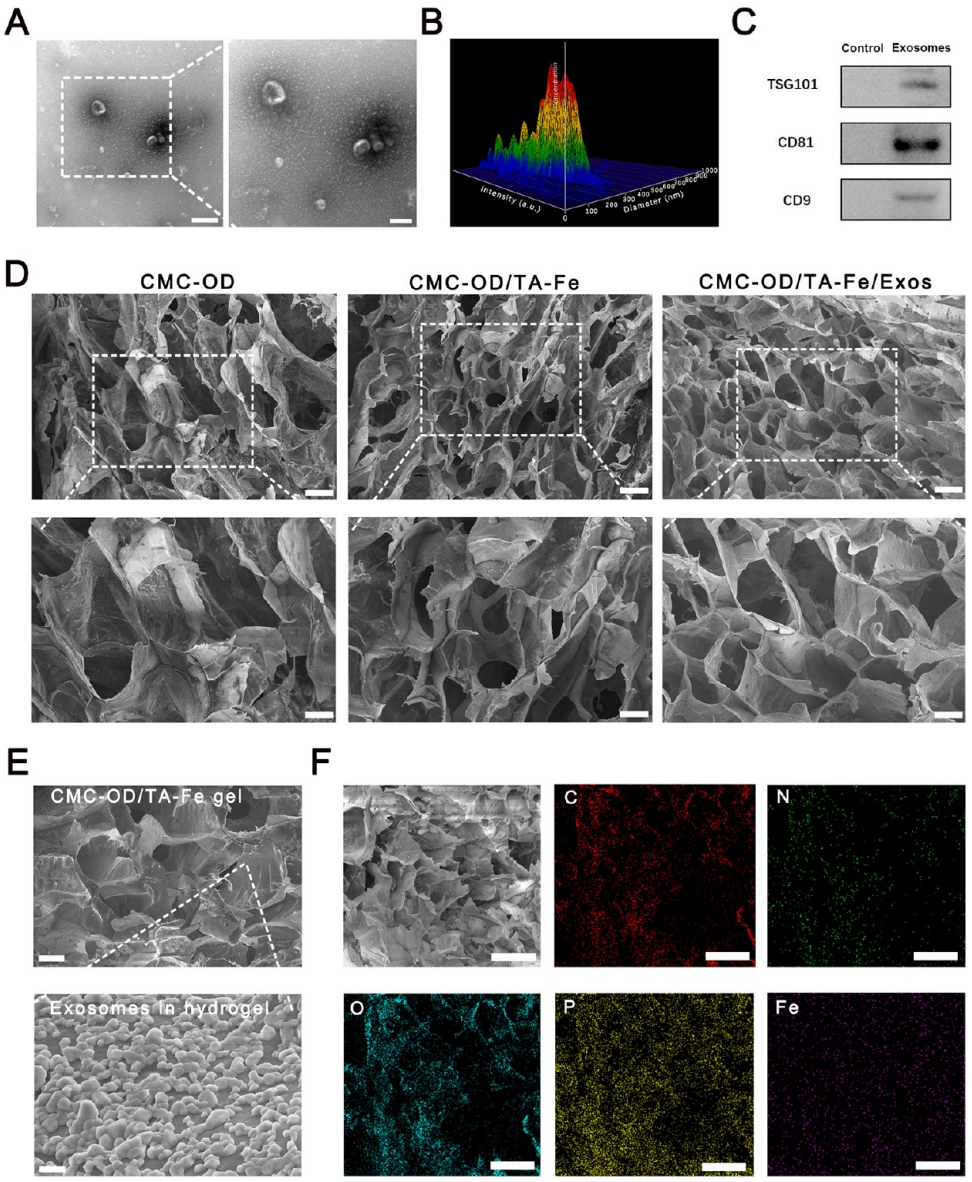

Figure 1. Evaluation of exosomes and hydrogel properties. (A) Transmission electron microscopy (TEM) imaging was employed to characterize the ultrastructural features of exosomes (scale bar: low: 200 nm, high: 100 nm). (B) Nanoscale exosomes sizing was performed via Nanoparticle Tracking Analysis (NTA) capturing Brownian motion trajectories. (C) Exosomal biomarkers (TSG101, CD9, CD89) were quantified via Western blotting to validate vesicle identity. (D) Micromorphology analysis of different hydrogels after freeze-drying by SEM (scale bar: low: 100 μm, high: 50 μm). (E) SEM microstructure of CMC-OD/TA-Fe/AEAA-Exos hydrogels and morphology of exosomes attached to the surface of hydrogels at high magnification (scale bar: low: 50 μm, high:1 μm). (F) Elemental energy spectrum analysis of CMC-OD/TA-Fe/AEAA-Exos hydrogels (scale bar: 250 μm). (n = 3).

Mesenchymal stem cells (MSCs) demonstrate multipotent differentiation capacity coupled with prolonged self-renewal potential, mitotic activity, immune homeostasis regulation, and marked inflammation-suppressing properties.[7,8] Human umbilical cord mesenchymal stem cells (hucMSCs) possess stable biological properties, are easy to obtain, are rich in sources, and have minimal ethical risks. MSC-secreted exosomes exhibit excellent antifibrotic activity.[9,10] Recent investigations into the pathogenesis of hepatic fibrosis have employed rodent models to evaluate the antifibrotic efficacy of exosomes originating from umbilical cord-derived MSCs and have shown that these exosomes have unique advantages against hepatic fibrosis.[11,12] In addition, exosomes, as natural vehicles, have been widely studied and applied in targeted drug delivery therapy, disease diagnosis, and as biomarkers for prognosis.[13−15] However, a critical limitation in exosome therapeutics lies in their accelerated clearance via the mononuclear phagocyte system following systemic administration.[16] This will result in a shortened circulation time of the therapeutic drug in the body, making it difficult to maintain an effective concentration, thereby reducing the efficacy. Therefore, the traditional approach of administering exosomes systemically via intravenous introduction cannot meet the therapeutic requirements of long-term preservation and sustained release in vivo.

Hydrogels, with their three-dimensional polymerization network structures, can simulate the tissue matrix in vivo and encapsulate exosomes for sustained release.[17,18] Carboxymethyl chitosan (CMC) has excellent water solubility and biological activity, and is used as a biomedical material.[19−21] Oxidized dextran (OD) not only retains the good biodegradability and

https://doi.org/10.1021/acsnano.5c06003
ACS Nano 2025, 19, 34575−34595

Scheme 1. Based on Schiff Base Reaction, a New Hydrogel CMC-OD/TA-Fe(III) Was Prepared by CMC, OD and TA-Fe(III)[a]

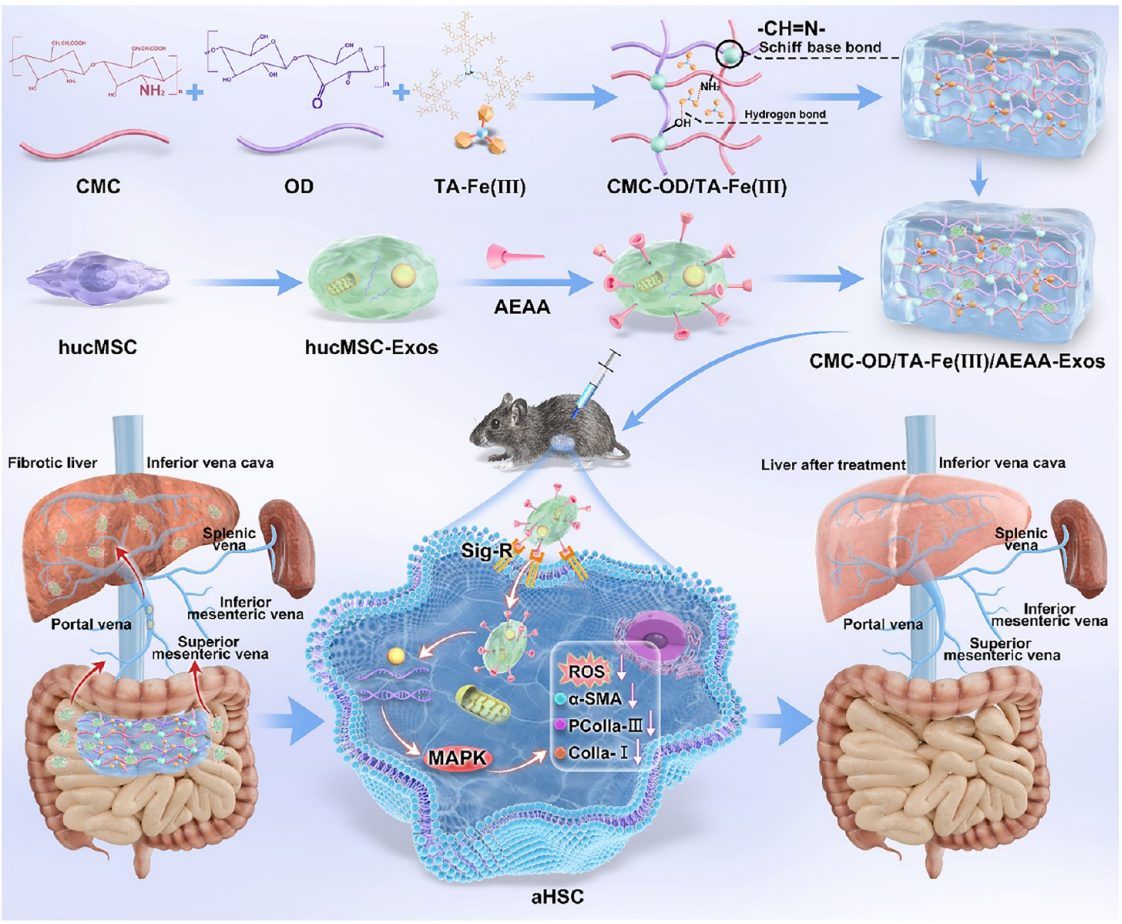

[a]hucMSCs derived exosomes were modified with AEAA. Then the AEAA-modified exosomes were encapsulated in the synthesized hydrogel. The hydrogel/exosome delivery systems were administered via intraperitoneal injection into C57BL/6J mice with hepatic fibrosis. This approach enabled sustained release of exosomes that specifically targeted activated hepatic stellate cells (aHSCs), suppressed the expression of α-SMA, Colla I and procollagen III (PColla III) through the MAPK pathway, and ultimately alleviated hepatic fibrosis.

biocompatibility of dextran, but also has a large number of aldehyde groups on the chain, which can quickly form a hydrogel with chitosan and provide strong tissue adhesion by reacting with tissue amines.[22] As a botanical polyphenol, tannic acid (TA) possesses a characteristic molecular architecture featuring abundant phenolic hydroxyl moieties accompanied by catechol and pyrogallol functional units.[23] These groups can be used in the preparation of hydrogels by cross-linking macromolecules through hydrogen, ionic, and coordination bonds as well as hydrophobic interactions.[24] The TA polyphenol group can rapidly combine with an amino group in body tissue through hydrogen bonding to achieve robust adhesion.[25] Additionally, as an essential trace element in the human body, Fe^{3+} ions can be chelated with digalloyl rich in TA at multiple points to form stable metal polyphenol complexes.[26] Metal polyphenols can enhance the structural stability of hydrogels and promote antibacterial and cell proliferation activities.[27] In this study, exosomes were loaded into hydrogels and injected into the abdominal cavity, where they could be directly absorbed by the mesenteric arteries and enter the liver through the portal vein. This drug delivery route can achieve sustained release and maximize exosomal access to the liver.

While exosomes possess intrinsic targeting ability toward pathological sites through surface adhesion molecules, their biodistribution kinetics in living systems often demonstrate suboptimal tissue-specific accumulation rates. The compromised targeting specificity of exosomes coupled with systemic dilution effects may significantly impair their biodistribution to pathological niches and their therapeutic efficacy.[28] This will cause the drug to fail to effectively accumulate in the diseased liver tissue/hepatic stellate cells, not only reducing the local therapeutic effect, but also potentially increasing the potential risk of side effects on other nontarget organs. As a high-affinity sigma receptor- (σR) targeting moiety, aminoethyl anisamide (AEAA) demonstrates preferential binding to activated hepatic stellate cells (aHSCs) where σR expression is upregulated, enabling selective cellular internalization, and has a high uptake efficiency by aHSCs.[29,30] Therefore, hucMSC-derived exosomes were vectorized with AEAA to specifically target activated stellate cells. In this study, CMC, OD, and iron tannate (TA-Fe (III)) were used to design metal polyphenol-based polymer hydrogels (CMC-OD-TA-Fe (III), Gel) with favorable stability and low cost, and hucMSC-derived exosomes modified with AEAA were encapsulated in hydrogels. The sustained-release exosomes were able to enter the liver through the portal vein system, avoiding systemic blood

https://doi.org/10.1021/acsnano.5c06003
ACS Nano 2025, 19, 34575−34595

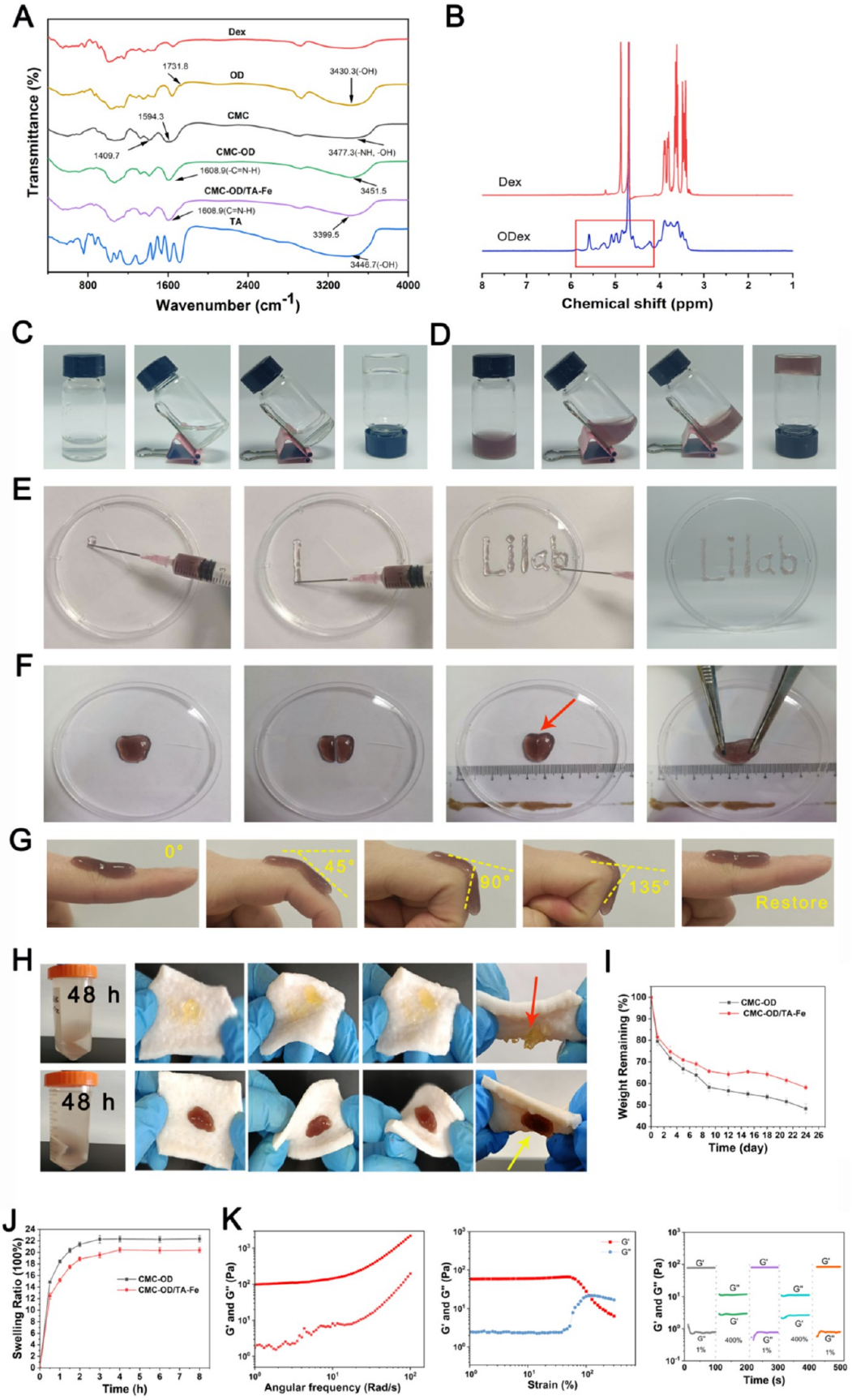

Figure 2. Characterization of hydrogels' synthesis and properties. (A) Fourier-transform infrared spectroscopy of hydrogel components. (B) ^{1}H NMR assay of dextran and oxidized dextran. (C, D) show the colloidal states of CMC-OD and CMC-OD/TA-Fe hydrogels, respectively. (E) Injectable ability test of CMC-OD/TA-Fe hydrogel. (F) Test of self-healing properties for CMC-OD/TA-Fe hydrogel. (G) Viscoelastic

https://doi.org/10.1021/acsnano.5c06003
ACS Nano 2025, 19, 34575−34595

Figure 2. continued

test of CMC-OD/TA-Fe hydrogel. (H) The adhesion properties of CMC-OD and CMC-OD/TA-Fe hydrogels were evaluated by porcine skin tests. (I) Analysis of degradation characteristics of hydrogels. (J) Analysis of swelling properties of hydrogels. (K) Rheological properties of CMC-OD/TA-Fe hydrogel were evaluated by angular frequency test, stress test and stepwise strain test, respectively. Data are presented as means ± SD (n = 3).

circulation and specifically targeting activated HSCs (aHSCs) to treat hepatic fibrosis, representing a new, safe, and efficient treatment strategy.

2. RESULTS AND DISCUSSION

2.1. Synthesis and Characterization of Hydrogels/Exosomes. MSC-exosomes demonstrate therapeutic potential in tissue regeneration through their unique paracrine signaling and proven efficacy in attenuating chronic hepatic injury.[31−33] The exosomes used in this study were secreted by hucMSCs. The specific extraction process of Wharton's jelly derived MSCs is described in the Supporting Information (Figure S1A). Figure S1B shows the growth status of first-, second-, and third-generation umbilical cord stem cells. The morphology of umbilical cord MSCs was clear and consistent with the characteristics of MSCs, and their growth status was good. We identified the surface markers of the extracted stem cells using two-color flow cytometry, as shown in Figure S1B. The positive antibody expression markers included CD90, CD73, and CD105, and the negative antibody expression markers included CD19, CD11b, CD34, and HLADR. The phenotypic identification results of the cells were consistent with those of umbilical cord stem cells in relevant literature,[34] which further confirmed that the hucMSCs were successfully extracted.

We characterized exosomes derived from hucMSCs (Figure 1A−C). As shown in Figure 1A, the exosomes were shown to be circular by scanning electron microscopy (SEM), and nanoparticle tracking analysis (NTA) showed that the particle size distribution of exosomes derived from hucMSCs was concentrated at approximately 135 nm (Figures 1B and S2). In addition, as shown in Figure 1C, the phenotype of hucMSCs derivatives was identified by Western blot, and the surface positive markers TSG101, CD81, and CD9 of derivatives showed clear bands (Figure 1C), proving that the umbilical cord MSC derivatives extracted and purified in this study were exosomes. Exosomes and AEAA-vectorized exosomes were characterized by ζ-potential (Table S1), and there was no significant difference in their potential. However, fluorescence colocalization test confirmed that AEAA successfully bound to the exosomes (Figure S19A). Transmission electron microscopy (TEM) images indicates that the AEAA modification does not cause significant damage to the integrity of the exosome membrane (Figure S19B). And the efficiency of exosomes carrying AEAA was calculated to be 72% in this study, also suggesting that AEAA and Exosomes can stably bind together.

After the prepared CMC-OD, CMC-OD/TA-Fe, and CMC-OD/TA-Fe/Exos hydrogel delivery systems were freeze-dried and sprayed with silver, the micromorphologies of the different groups were observed using SEM. We found that the different groups of hydrogels were loose and porous. Compared with the CMC-OD system, the pore sizes of the CMC-OD/TA-Fe and CMC-OD/TA-Fe/Exos hydrogel delivery systems were slightly smaller and more uniform. This may be because TA-Fe, as a metal polyphenol, improves the mechanical properties of the hydrogel and enhances its structural strength.[21,27,35,36] However, after the exosomes were encapsulated in the CMC-OD/TA-Fe hydrogel, the structure of the hydrogel did not change significantly (Figure 1D), indicating that the physical and chemical properties of the CMC-OD/TA-Fe hydrogel did not change after encapsulation. The stability of the exosomes was also ensured, which was conducive to the stable exosome release curve of the hydrogel. High magnification showed that many exosomes were attached to the hydrogel surface (Figure 1E). Elemental energy spectrum analysis was performed on the hydrogels containing exosomes, and C, N, O, P, and Fe were present in the CMC-OD/TA-Fe/AEAA-Exos gel (Figure 1F). Because iron tannate contains Fe, this preliminarily indicated the synthesis of the CMC-OD/TA-Fe hydrogel. The presence of N and P may be related to the presence of AEAA-exosomes inside the hydrogel, whose membranes are composed of a phospholipid bilayer, the surface of which is inlaid with transmembrane proteins.[37,38] In this study, based on the Schiff base reaction, the amino group of CMC and the aldehyde group of OD formed an imine bond (−RC═N−), and the hydrogel was synthesized,[39,40] as shown in Scheme 1. Dextran was oxidized to OD by sodium periodate, which increased the number of carbonyl groups (−RC═O), thus enhancing the cross-linking properties of CMC and OD.[41−43]

In this study, the oxidation degree of OD was measured to be 40%. As shown in Figure 2A, The modified chitosan exhibited two distinctive spectral features centered at wavenumbers 1409.7 and 1594.3 cm^{-1} in Fourier-transform infrared spectroscopy (FTIR) characterization.[44] The optical density spectrum of OD is very similar to that of dextran, because the vibration absorption peak of the aldehyde group is very similar to that of dextran. After oxidation, dextran has a new absorption peak at 1731.8 cm^{-1}, which is close to the previous peak at 1732 cm^{-1}.[42,45,46] The emergence of this new absorption peak was the result of the stretching vibration of C═O in the aldehyde group of dextran after oxidation.[47] Proton nuclear magnetic resonance (^{1}H NMR) showed that compared with the spectrum of preoxidized dextran, the OD spectrum had several additional peaks in the chemical shift range of 4.2−5.8 ppm (Figure 2B), and they were assigned to the proton of the hemiacetal structure.[48] The above analyses verified the effective oxidation of dextran, evidenced by significant aldehyde group generation.

The absorption bands of −OH in OD and -NH_2 in CMC at 3430.3 and 3477.3 cm^{-1}, respectively, converged to 3451.5 cm^{-1} in the CMC-OD gel (Figure 2A), indicating that −NH_2 in the CMC molecular chain interacted with −OH in OD to form hydrogen bonds. In the spectrum of the CMC-OD hydrogel, a characteristic peak of an imine bond appears at 1608.9 cm^{-1} (Figure 2A), indicating that the Schiff base reaction occurred between −NH_2 of CMC and −CH═O of OD. The absorption bands of 3446.7 cm^{-1} in TA and 3451.5 cm^{-1} in the CMC-OD gel correspond to that of −OH (Figure 2A), which migrated to 3399.5 cm^{-1} in the CMC-OD/TA-Fe hydrogel, indicating that the TA-Fe complex results in the generation of hydrogen, ionic, and coordination bonds in the synthesis of CMC-OD/TA-Fe hydrogels.[49]

https://doi.org/10.1021/acsnano.5c06003
ACS Nano 2025, 19, 34575−34595

2.2. Injectable, Self-Healing, and Viscoelastic Analyses of Hydrogels. CMC-OD and CMC-OD/TA-Fe hydrogels were prepared in transparent ampules. The CMC-OD hydrogels were colorless and transparent (Figures 2C and S3) and purple-brown after the addition of TA-Fe (Figures 2D and S3). The gelation times of the two hydrogels were measured via the inverted vial technique, and both were less than 1 min; moreover, the gelation time of CMC-OD/TA-Fe was shorter than that of CMC-OD (Figure S3), indicating that the addition of TA-Fe promoted cross-linking of the hydrogels,[27] shortening the gelation time. This result indicated that CMC-OD/TA-Fe can meet clinical needs in terms of gelation time. We used a 5 mL syringe to test the injectability of the CMC-OD/TA-Fe hydrogel, and wrote "Li lab" in a 10 cm confocal dish. Finally, the confocal dish was set on its edge, and it was observed that "Li lab" never fell off the gel (Figure 2E). During the operation, the injection gel was pushed smoothly by the syringe, indicating that CMC-OD/TA-Fe had good injectability, which laid the foundation for subsequent intraperitoneal injections.

The self-healing test was conducted as shown in Figure 2F. First, the prepared heart-shaped CMC-OD/TA-Fe hydrogel was divided into two parts with a blade, and then merged together. After 30 min, the hydrogel was stretched on both sides with an appropriate force using tweezers. The hydrogel did not separate at the fracture, indicating that it had good self-healing properties. CMC-OD/TA-Fe hydrogel was injected into an index finger, which was bent at different angles (0, 45, 90, and 135°), and finally recovered (Figure 2G). The bending and adhesion of the hydrogel on the surface of the index finger were good, indicating favorable viscosity and elasticity. In addition, we explored the elasticity and tissue adhesion of the CMC-OD/TA-Fe hydrogels through porcine skin twisting experiments and evaluated the adaptability of the hydrogels to complex environments, such as intestinal peristalsis in the abdominal cavity. Neither the CMC-OD nor CMC-OD/TA-Fe gels broke or fell off the porcine skin after it was twisted in different directions (Figure S4). The porcine skin attached to the gel was then soaked in 0.9% normal saline for 24 h, removed, twisted in different directions, and inverted. The CMC-OD gel was broken, and only a small part remained attached to the porcine skin (Figure 2H, red arrow). The CMC-OD/TA-Fe gel was intact and did not break off from the porcine skin (Figure 2H, yellow arrow). The livers, spleens, and kidneys of SD rats were divided into two parts with a blade, and then glued back together hydrogel. After 10 min, the tissues were suspended, and all glued organs firmly held together without separation (Figure S5a−c). However, the CMC-OD gel-bonded liver tissue showed a significant separation (Figure S5d). These results suggested that, compared with the CMC-OD gel, the CMC-OD/TA−Fe hydrogel had superior elasticity and adhesion to tissues, making it a more favorable hydrogel/exosome delivery system for the sustained release of exosomes. In addition to its ability to cross-link with other polymers to form gels, OD has an important advantage. That is, hydrogels containing OD can extend to the irregular surfaces of damaged tissue, thereby promoting adhesion to epithelial cells.[50] The hydrogen bond in TA has a good binding effect with tissue $-NH_2$,[25] which enhances the adhesion of TA to tissues. Guo et al. revealed that the higher the TA content, the higher the number of polyphenol groups and cross-linking density, which further enhances the interface adhesion and cohesion of hydrogels.[51] In addition, balancing the cohesion and adhesion of injectable hydrogels while maintaining their fluidity is important to obtaining strong adhesion.[52] The above description may be the main reason why CMC-OD/TA-Fe exhibits good organizational adhesion.

2.3. Degradation, Swelling, and Encapsulation Rate Analysis of Hydrogels. As shown in Figure 2I, compared to that of the CMC-OD hydrogel, the degradation rate of the CMC-OD/TA-Fe hydrogel was not significantly different at the early stage of degradation, but the gap gradually increased after 4 days of degradation and remained constant after 14 days. The degradation rates were faster in the first 10 days and gradually slowed over time. The degradation rate of CMC-OD/TA-Fe hydrogel was slower than that of CMC-OD gel, which may be because the TA-Fe complex strengthened the gel structure. As shown in Figure 2J, CMC-OD hydrogel reached a stable state at 3 h, and the swelling stability time of CMC-OD/TA-Fe hydrogel was slightly longer, while comparative hydrogel performance evaluation showed inverse proportionality between metal-phenolic coordination density and equilibrium swelling ratios across the tested formulations. This phenomenon also indicated that TA-Fe incorporation induced structural densification in CMC-OD networks, which reduced maximum swelling indices, and CMC-OD/TA-Fe hydrogel had stronger structural strength than that of CMC-OD gel, which is consistent with the degradation characteristics of the hydrogels, as shown in Figure 2I. Existing literature consistently demonstrates that CMC[44,53] and OD[54] have good degradation properties, which is an important factor for the formation of hydrogels that encapsulate exosomes for sustained drug release. And it was determined that the encapsulation rate of exosomes by the hydrogel was 96.8%.

2.4. Analysis of Rheological Properties of CMC-OD/TA-Fe Gel. Figure 2K shows that the storage modulus of the CMC-OD/TA−Fe hydrogel was 1000 pa. In Figure 2K, the two curves intersect at a strain of 113%. The sudden decrease in the storage modulus G' and sudden increase in the loss modulus G'' at the strain point indicated that the internal structure of the hydrogel was damaged, and the hydrogel changed from a solid to a liquid state with fluid characteristics.[55,56] Compared with the single cross-linked hydrogel of CMC and OD reported by Li et al.,[39] CMC-OD/TA-Fe hydrogels showed a higher critical strain, verifying that multiple cross-linked hydrogels could withstand greater deformation to meet the needs of complex abdominal cavity environments. We further evaluated the self-healing behavior of the CMC-OD/TA−Fe hydrogel by applying oscillatory strain at a frequency of 1 Hz and range of 1−400%. First, a 1% strain was applied to maintain the colloidal nature of the CMC-OD/TA−Fe hydrogel. After 100 s, a larger strain of 400% was applied, and the G' value became smaller than before, whereas the G'' value became larger than before. The dominance of the loss modulus (G'') over the storage modulus (G') signified structural disintegration of the hydrogel network; however, upon strain reduction from 400% to 1%, both moduli exhibited complete recovery to their initial values. These results illustrated that the hydrogel recovered its structural integrity after continuous stepwise strain and exhibited strong self-healing capability. This is related to the fact that CMC-OD/TA-Fe is composed of Schiff bases and coordination bonds, both of which are dynamic bonds.[56]

2.5. Analysis of State and Slow-Release Properties of Exosomes Encapsulated in Hydrogel. Figure S6A shows

https://doi.org/10.1021/acsnano.5c06003
ACS Nano 2025, 19, 34575−34595

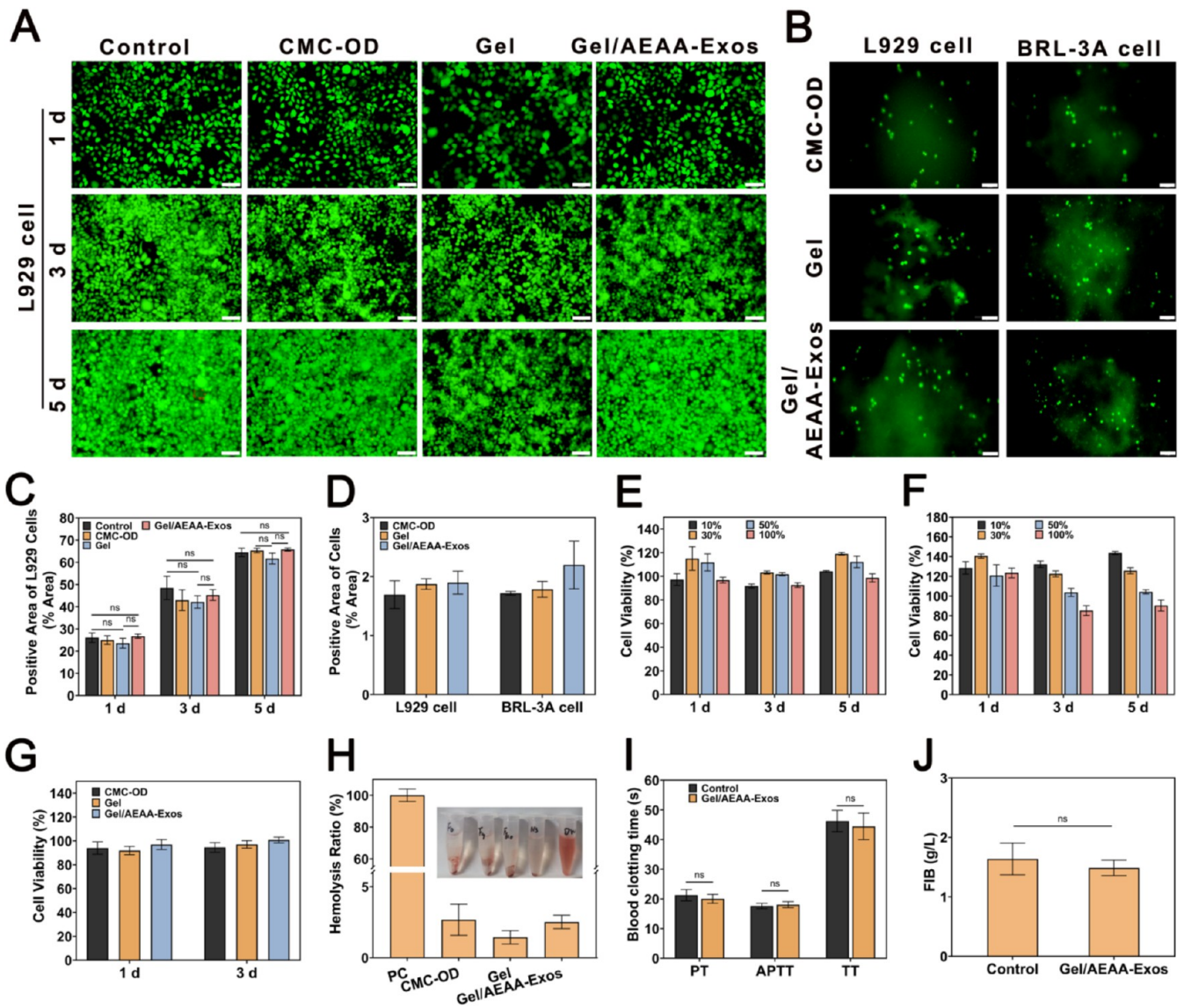

Figure 3. In vitro biosafety assessment of hydrogel/exosome systems. (A) Live and dead stain results of L929 cells treated with different groups of hydrogel extracts (scale bar: 100 μm). (B) Adhesion tests of L929 cells and BRL-3A cells grown on different hydrogel surfaces (scale bar: 100 μm). (C) Quantification analysis of the live L929 cell-positive expression area by ImageJ software correspond to (A). (D) Quantification analysis of the live L929 and BRL-3A cells-positive expression area by ImageJ software correspond to (B). (E) CCK-8 cytotoxicity assay of hydrogels on L929 cells. (F) CCK-8 cytotoxicity assay of hydrogels on BRL-3A cells. (G) CCK-8 cytotoxicity assay of different hydrogels on BRL-3A cells by CCK-8 cytotoxicity assay. (H) Assessment for the effect of hydrogels on hemolysis. (I, J) Assessment for the effects of hydrogel coagulation. Data are presented as means ± SD (n = 3). P > 0.05 (ns, not significant).

uniformly dispersed exosomes labeled in red with PKH-26 fluorescent dye. In terms of macroscopic morphology, the exosomes before and after labeling were encapsulated in CMC-OD/TA-Fe hydrogel (Gel/PKH-26-Exos) in a brown transparent jelly state (Figure S6B). Through confocal 3D imaging, we observed that exosomes encapsulated in hydrogels remained abundant after storage at 4 °C for 3 and 72 h, while unlabeled exosomes (control group) were not observed (Figure S6C). The fluorescence intensity of the PKH-26-labeled exosomes encapsulated in hydrogels was quantified, and the red fluorescence intensity was lower after 72 h than after 3 h (Figure S6D), which may be related to the gradual weakening of the fluorescence intensity over time. In conclusion, this experiment suggested that the exosomes encapsulated in the CMC-OD/TA-Fe hydrogels were stable. According to the sustained-release curve of the exosomes (Figure S6E), the release rate was high in the first 4 days and gradually slowed down afterward. The release rate was 55.8% on the fourth day, and then gradually stabilized, reaching 79.8% on the 28th day.

2.6. Biocompatibility Analysis of Hydrogel/Exosome Delivery Systems In Vitro. Biocompatibility relates to the phenomena that occur during interactions between materials and hosts and is essential for the material to function in clinical application.[57] First, the L929 cell viability after hydrogel exposure was quantitatively assessed using fluorescence-based live/dead staining (calcein−AM/PI). The numbers of cells in the different groups gradually increased with time, but neither cell morphology nor survival activity showed significant changes in the different groups at different times (Figure 3A,C). At the same time, we tested the activity of different groups of hydrogels on BRL-3A cells. Comparative analysis

https://doi.org/10.1021/acsnano.5c06003
ACS Nano 2025, 19, 34575−34595

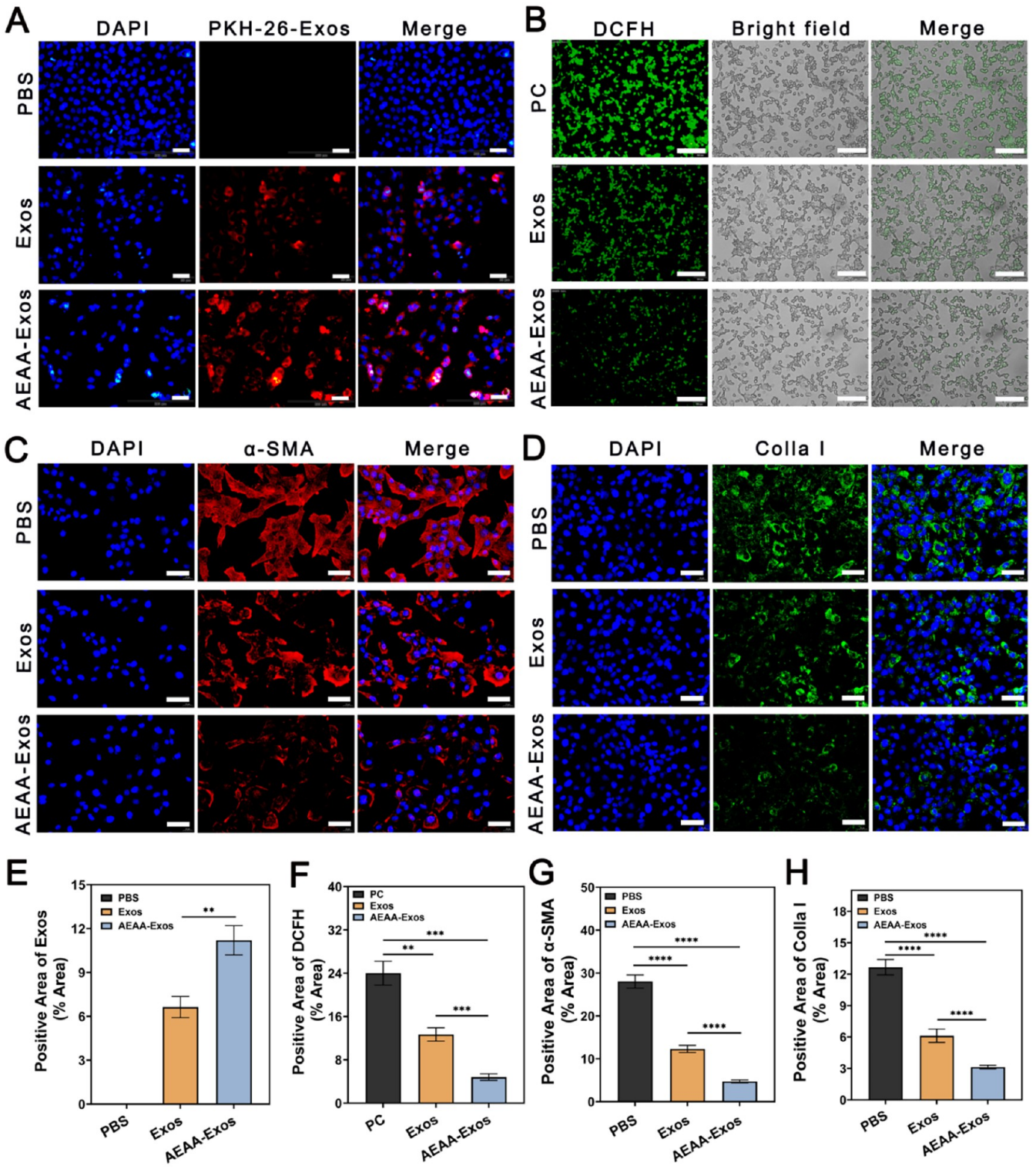

Figure 4. Evaluation of biological function of hydrogel/exosome systems in vitro. (A) Evaluation of targeting of activated hepatic stellate cells by gel/AEAA-Exos systems (scale bar: 50 μm). (B) Evaluation of anti-ROS ability in gel/AEAA-Exos systems (scale bar: 400 μm). (C) The antifibrotic effect of gel/AEAA-Exos systems was evaluated by α-SMA index (scale bar: 100 μm). (D) The antifibrosis effect of gel/AEAA-Exos systems was evaluated by Colla I index (scale bar: 100 μm). Quantification analysis of exosomes-positive area(E), DCFH-positive area (F), α-SMA-positive area (G) and Colla I-positive area (H). Data are presented as means ± SD (n = 3). **P < 0.01, ***P < 0.001, ****P < 0.0001.

revealed comparable morphological features across the different groups, all of which were spindle-shaped or irregular, and the cell number in the Gel/AEAA-Exos group was not significantly different from that in the control group (Figure S7A,B). In addition, L929 and BRL-3A cells were cultured on the surfaces of CMC-OD, Gel and Gel/AEAA-Exos hydrogels for adhesion experiments. After 24 h of culture, the growth state of the two cell types in the different hydrogel groups was

https://doi.org/10.1021/acsnano.5c06003
ACS Nano 2025, 19, 34575−34595

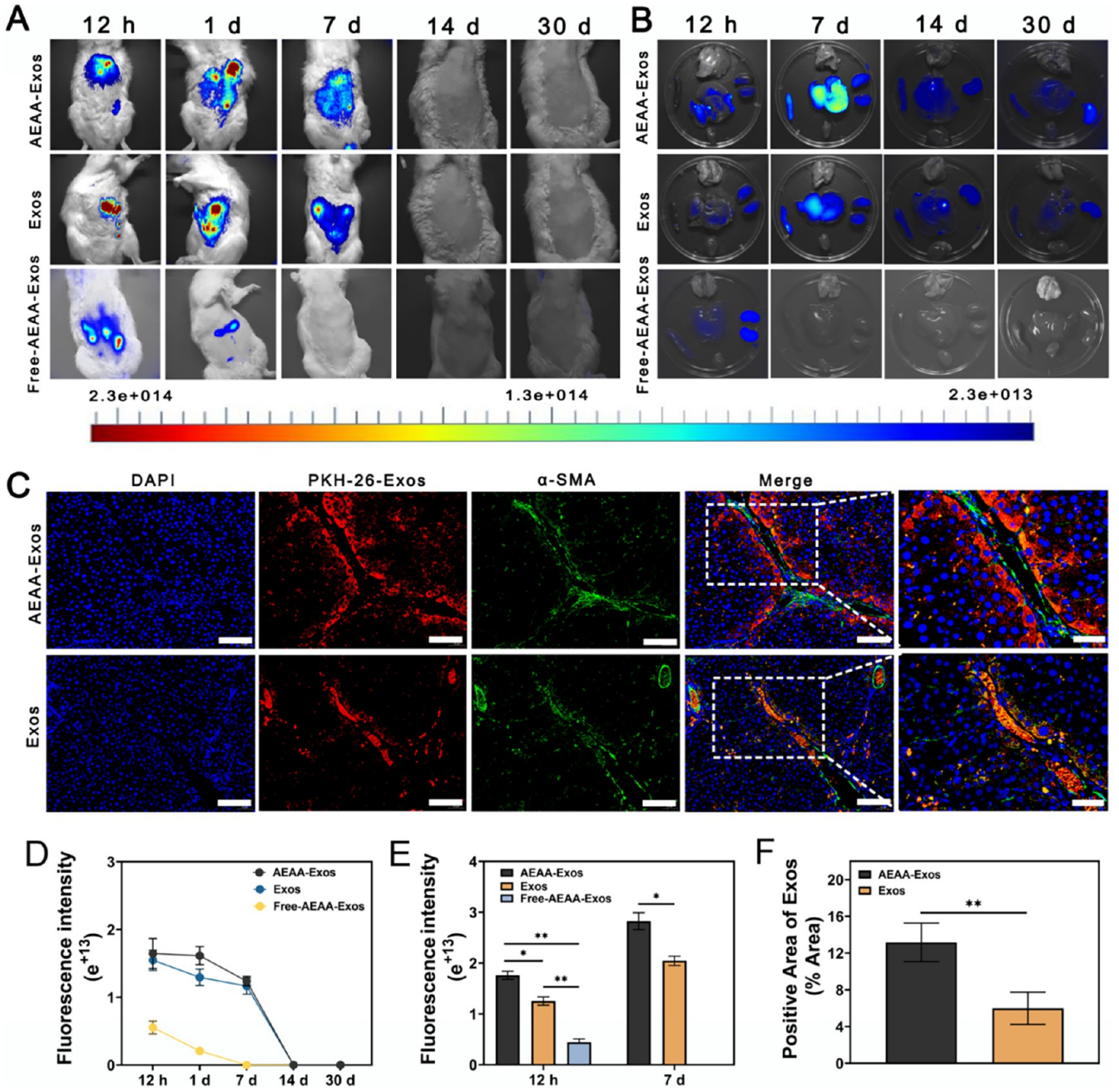

Figure 5. Evaluation of in vivo targeting ability of hydrogel/exosome systems. (A) Small animals imaging results of after free AEAA-exosomes (Free-AEAA-Exos group), gel/Exos (Exos group) and gel/AEAA-Exos (AEAA-Exos group) systems implantation in SD rats at different observation points (12 h, 1 day, 7 days, 14 days, 30 days). (B) Evaluation of the distribution of exosomes in the liver after free AEAA-exosomes, gel/Exos and gel/AEAA-Exos systems implantation in SD rats at different times (12 h, 7 days, 14 days, 30 days). (C) After gel/PKH-26-Exos system implantation in SD rats for 7 days, the targeting performance of exosomes on activated hepatic stellate cells was evaluated by tissue immunofluorescence assay (scale bar: low: 100 μm, high: 40 μm). (D) Fluorescence quantitative analysis of the distribution of exosomes in SD rats in vitro corresponding to (A). (E) Fluorescence quantitative analysis of the distribution of exosomes in the liver of SD rats in vivo corresponding to (B). (F) Quantification analysis of the distribution of exosomes in the liver of SD rats corresponding to (C). Data are presented as means ± SD ($n \geq 3$). *$P < 0.05$,$P < 0.01$.**

good (Figure 3B). The population counts as determined by fluorescence intensity of murine-derived L929 and rat-derived BRL-3A cells grown on the surfaces of hydrogels did not significantly differ after 24 h of culture in the different hydrogel groups (Figure 3D).

Subsequently, biocompatibility assessment was performed per ISO 10993−5 using the CCK-8 reagent with hydrogel extracts. Cells were cultured with Gel/AEAA-Exos hydrogel extract, and the viability of L929 and BRL-3A cells at different concentrations (10, 30, 50, and 100%) after 1, 3, and 5 days was above 91.7% (Figure 3E) and 84.3% (Figure 3F), respectively. At the same time, we cultured L929 cells with 100% hydrogel extract from different groups for 1 and 3 days and found that cell viability was above 91.8% (Figure 3G). The hydrogels were graded according to ISO 10993−5:19993660.[58] When cell viability was in the range of 80−

https://doi.org/10.1021/acsnano.5c06003
ACS Nano 2025, 19, 34575−34595

100%, the cytotoxicity rating was 0 (Table S2), and the cytotoxicity rating of the hydrogel materials in this study met the standard of grade 0. The experimental results showed that Gel/AEAA-Exos exhibited good biosafety. In addition, hemolysis and coagulation experiments were conducted to further explore the biosafety of the hydrogels. In the hemolysis experiment (Figure 3H), the solutions in 1.5 mL EP tubes corresponding to the Gel and Gel/AEAA-Exos groups were almost colorless and transparent, while the solution of the positive control group (red blood cells dispersed in deionized water in the EP tube labeled "DW") was obviously uniform red. The hemolysis rates in the Gel and Gel/AEAA-Exos groups were below 5%. These results indicated that Gel and Gel/AEAA-Exos exhibited good biosafety. In the coagulation tests (Figure 3I–J), none of the indices (PT, APTT, TT, or FIB) of Gel/AEAA-Exos significantly differed from those of the control group ($P > 0.05$). In conclusion, the above experiments showed that the hydrogel and Gel/AEAA-Exos delivery systems in this study had good biosafety and are suitable for clinical applications as medical materials.

2.7. In Vitro Targeting Analysis of Gel/AEAA-Exos Delivery Systems. To improve the effectiveness of exosome therapy, this study used AEAA to engineer exosomes derived from hucMSCs so that the exosomes could target and bind the sigma receptors on the surfaces of activated HSCs.[29,30] By analyzing the number of exosomes taken up in aHSCs and AML-12 cells, the targeting properties of AEAA-functionalized exosomes were evaluated. First, perinuclear localization analysis revealed that, compared with the nonvectorized exosomes (Exos) group taken up by HSC-T6 cells and AEAA-vectorized exosomes taken up by AML-12 cells a more abundant crimson-stained microparticles clustered around the nuclei of aHSCs in the AEAA-vectorized exosomes (AEAA-Exos) group (Figures 4A and S8A). The quantitative results suggested AEAA-modified exosomes have significant targeting properties toward aHSCs (Figures 4E, S8B, and S9). According to the previous research results,[29] the key to the targeting property of AEAA-modified exosomes lies in the fact that AEAA can bind to the Sigma receptor expressed on the surface of activated hepatic stellate cells. Both the cell immunofluorescence experiment and flow cytometry showed that, compared with the group without AEAA blocking, the amount of AEAA-Exos ingested by aHSCs blocked with AEAA was significantly reduced (Figures S8 and S10). This proved that the targeting ability of AEAA is mediated by the Sigma receptor on the surface of aHSCs.

2.8. In Vitro Anti-ROS and Antifibrosis Analysis of Gel/AEAA-Exos Delivery Systems. As shown in Figure 4B, the anti-ROS effect of exosomes vectorized with AEAA was detected by using a DCFH-DA probe. Green fluorescence was observed in aHSCs in the positive control (PC), Exos, and AEAA-Exos groups (Figure 4B), because more reactive oxygen species (ROS) in the cells oxidized DCFH-DA to DCFH, which shows green fluorescence. Both fluorescence quantitative analysis (Figure 4F, $P < 0.001$) and flow cytometry (Figure S11, $P < 0.05$) confirmed that, compared with nonvectorized exosomes, AEAA-vectorized exosomes significantly reduced ROS levels from a HSCs.

In addition, we evaluated the therapeutic effects of vectorized exosomes on fibrosis in vitro by examining the effects of different treatments on the levels of α-SMA and Colla I expressed by aHSCs. We found that red fluorescence signals corresponding to α-SMA (Figure 4C) and green fluorescence signals corresponding to Colla I (Figure 4D) were distributed around the blue nuclei in the different groups. The fluorescence quantitative analyses of α-SMA (Figure 4G) and Colla I (Figure 4H) both demonstrated that compared with nonvectorized exosomes, engineered exosomes demonstrated enhanced efficacy in suppressing α-SMA and Colla I expression in aHSCs ($P < 0.0001$). Besides, RT-PCR analyses indicated the mRNA expression levels of α-SMA ($P < 0.01$) and Col1a1 ($P < 0.05$) in the AEAA-Exos group were significantly lower than those in the Exos group (Figure S12). In vitro experiments demonstrated that the gel/AEAA-Exos delivery system significantly attenuated ROS accumulation and suppressed fibrotic activity.

2.9. In Vivo Targeting Analysis of Hydrogel/Exosome Delivery Systems. To further evaluate the targeting ability of the gel/AEAA-Exos delivery system, we implanted free AEAA-exosomes, gel/Exos and gel/AEAA-Exos in SD rats and evaluated exosome intake in the three groups at different time points using a small-animal imaging instrument. First, a hepatic fibrosis model was established, as shown in Figure S13. HE, Masson, and sirius red staining of the livers revealed that the hepatic tissues of the Model group had obvious hepatocyte necrosis and formed circular fibrotic bands, whereas the Normal group had no fibrotic bands. The successful establishment of a hepatic fibrosis model in SD rats was verified by these experimental findings.

After implantation of the hydrogel/exosome delivery system, the area covered by the exosome signal gradually expanded from 12 h to 7 days, over which time the number of exosomes released by the hydrogel gradually increased, and the exosomes gradually diffused to the surrounding tissues (Figure 5A). However, the free AEAA-exosomes initially showed a diffuse distribution pattern. Besides, after the 1th days of implantation, it was also showed that the amount of accumulated exosomes in rats in Free-AEAA-Exos group was significantly reduced compared to the Gel/Exos group and the Gel/AEAA-Exos group. After the seventh days of implantation, the free exosomes basically disappeared as shown in Figure 5A,D,E, and the same result was observed in the enrichment of the liver (Figure 5B). It indicates that the hydrogel/exosome system has a good sustained-release effect compared with free exosomes.

After anesthesia, we removed the hearts, lungs, livers, spleens, and kidneys of the rats. As shown in Figures 5B,D and S14, observation using a small-animal imaging instrument showed that compared with the Gel/Exos group, the exosomes in the Gel/AEAA-Exos group were distributed the most in the liver, while the distributions in the spleens, kidneys, hearts and lungs were less. After the seventh days of implantation, the free exosomes had almost completely disappeared in the liver and other organs. This suggested that the exosomes modified by AEAA have a targeting function and can efficiently accumulate at the fibrosis liver. In biodistribution studies of exosomes across animal models, Elisa et al. demonstrated predominant hepatic tissue accumulation of these extracellular vesicles, exhibiting significantly higher tropism compared to other organ systems.[39] The accumulation in the liver reached a maximum 7 days after implantation of the hydrogel/exosome delivery system (Figure 5B). However, the in vitro release experiments demonstrated a continuous release duration of up to 28 days (Figure S6E). This is because the in vivo environment (such as enzymatic degradation) significantly accelerates the degradation of the hydrogel and the release/clearance of exosomes. It was found that the volume of exosomes released in the first 7

https://doi.org/10.1021/acsnano.5c06003
ACS Nano 2025, 19, 34575–34595

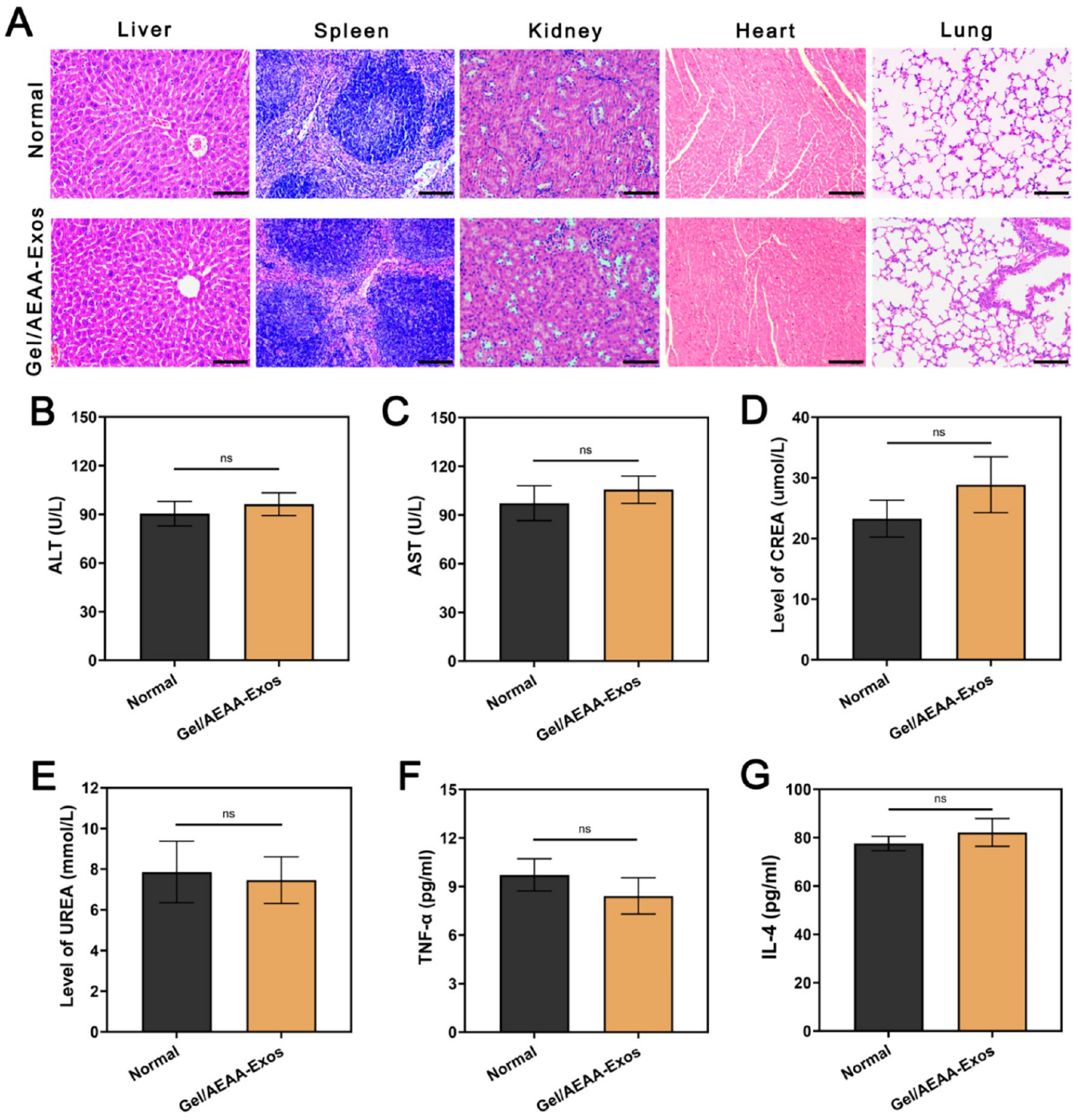

Figure 6. Biosafety evaluation of hydrogel/exosome systems in vivo. (A) HE stain pictures of liver, spleen, kidney, heart and lung of Normal group and experimental group after gel/AEAA-Exos implantation in mice for 7 days (scale bar: 400 μm). (B−E) evaluated the biosafety of gel/AEAA-Exos systems was evaluated by serum ALT, AST, CREA and UREA levels, respectively. (F, G) The biosafety of gel/AEAA-Exos system was evaluated by ELISA kit for serum TNF-α and IL-4 levels, respectively. (n = 5). P > 0.05 (ns, not significant).

days was 59.3%. This indicates that the rapid release phase in the early 7 days in vitro may be the main factor driving the 7-day peak effect in the body. It helps maintain a local effective concentration, prolong the treatment window. Regarding the phenomenon that free exosomes quickly disappear in the abdominal cavity, this might be related to the fact that exosomes lack the protection of hydrogels, making them vulnerable to being disrupted by the microenvironment within the abdominal cavity, as well as their rapid distribution throughout the body and subsequent consumption. In all, the above results illustrated that vectorized exosomes had better targeting ability against fibrotic liver tissues than did non-vectorized exosomes, the hydrogel played a crucial role in the sustained release of exosomes.

According to previous studies, aHSCs can produce collagen fibers, including α-SMA.[60] Therefore, α-SMA was used as the marker for aHSCs in this study. We collected liver tissues from rats 7 days after injection with Gel/Exos and Gel-AEAA-Exos and conducted tissue immunofluorescence analysis. In the Gel/AEAA-Exos group, many exosomes (red fluorescence

https://doi.org/10.1021/acsnano.5c06003
ACS Nano 2025, 19, 34575−34595

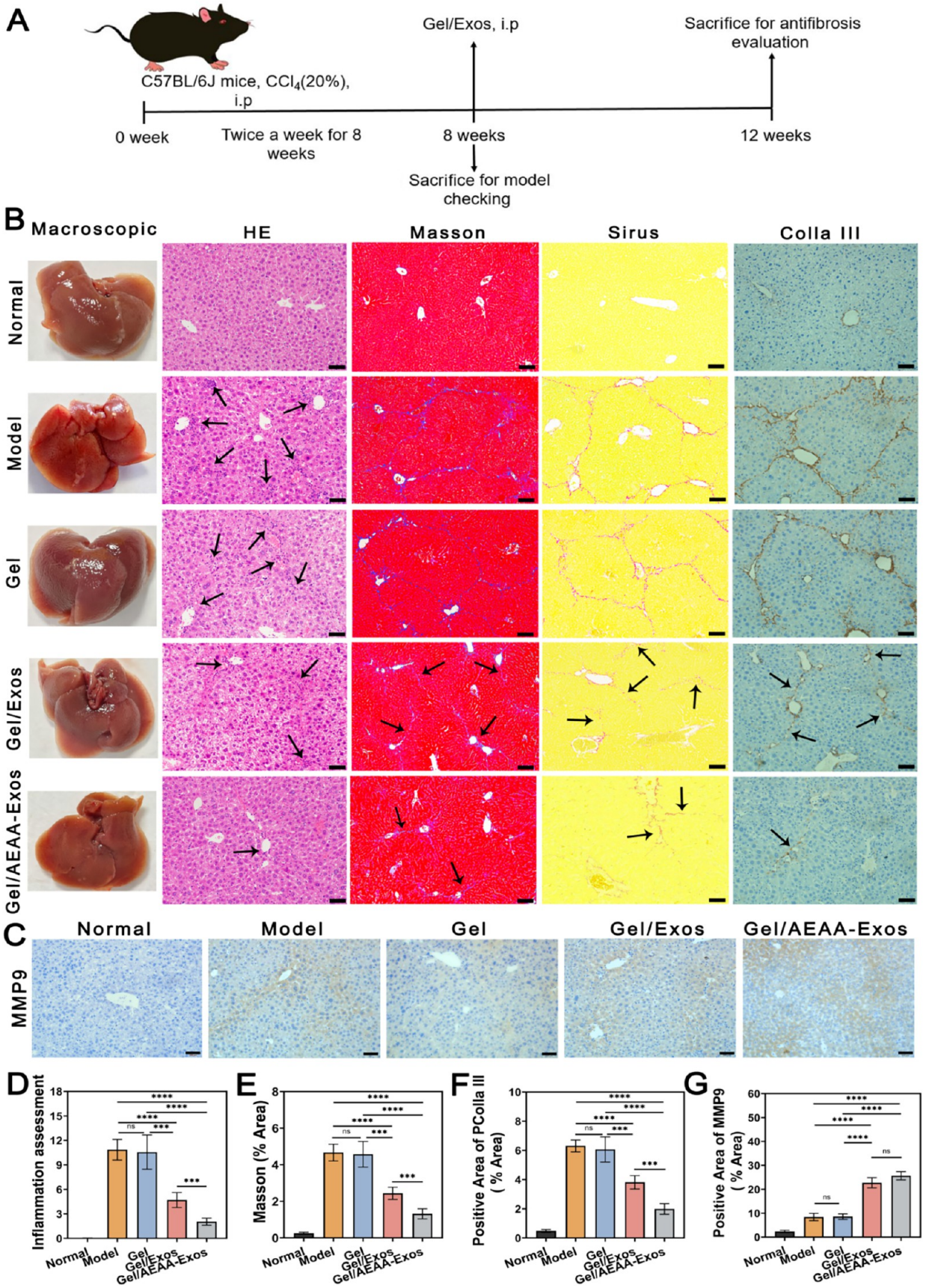

Figure 7. Evaluation of in vivo antifibrosis ability of hydrogel/exosome systems. (A) The process of establishing hepatic fibrosis modeling and antihepatic fibrosis is shown. (B) To evaluate the antifibrosis effect of gel/AEAA-Exos systems by HE, Masson, sirius red stain and PColla III (scale bar: 200 μm). (C) The antifibrosis effect of gel/AEAA-Exos system was evaluated by MMP9 index (scale bar: 200 μm).

https://doi.org/10.1021/acsnano.5c06003
ACS Nano 2025, 19, 34575−34595

Figure 7. continued

Quantification analysis of inflammation-positive area (D), Masson-positive area (E), PColla III-positive area (F) and MMP9-positive area (G). Data are presented as means ± SD (n = 5). ***P < 0.001, ****P < 0.0001, P > 0.05 (ns, not significant).

signal) accumulated around α-SMA (green fluorescence signal). However, the red signal around α-SMA in the Gel/Exos group was relatively small (Figure 5C). Quantification of exosomes-positive area demonstrated the significantly enhanced exosome localization efficiency of the AEAA-modified hydrogel composites compared to that in conventional exosome-loaded gels (Figure 5F), again indicating that vectorized exosomes had better targeting performance than did nonvectorized exosomes. Recently, both Hu and Zhang's studies have confirmed that the vectorized nanoparticles of AEAA have a significant targeting effect on aHSCs.[61,62] Furthermore, it was also suggested that the AEAA-exosomes released by the hydrogel can enter the intestinal tissue through the blood circulation and be metabolized in the intestinal tissue in this study (Figure S15).

2.10. In Vivo Degradation and Biosafety Analysis of the Hydrogel/Exosome Delivery System. As shown in Figure S17, it was found that within 30 days, although the hydrogel has undergone a large amount of degradation, it has not yet been completely degraded, which initially indicated that its degradation characteristics provide a guarantee for its sustained release function during one month. During the observation period, the rats were in good condition. Moreover, after the hydrogel/AEAA-Exos system implantation into the SD rats for 30 days, gastrointestinal system was smooth and well-expanded, with no obvious obstructions or intestinal adhesion (Figure S20). This initially confirmed the excellent safety performance of the hydrogel/exosome delivery system.

We further evaluated the biosafety of the hydrogel/exosome delivery system using hematoxylin and eosin (HE)-stained histomorphological images and serological detection. Histopathological evaluation demonstrated preserved hepatic architecture in the Gel/AEAA-Exos group, with intact hepatocyte morphology, physiological lobular organization, and baseline inflammatory cell profiles comparable to those of Normal controls (Figure 6A). Parenchymal cell morphologies in other organs, such as the spleen, kidneys, lungs, heart (Figure 6A), and brain (Figure S9), as well as inflammatory cell infiltration were not significantly different in the experimental and Normal groups. The corresponding ALT, AST, CREA, and UREA kits were used to detect the levels of serological indicators in the Gel/AEAA-Exos and Normal groups, and no significant differences were observed (P > 0.05). We also determined TNF-α and IL-4 levels with an enzyme-linked immunosorbent assay (ELISA) kit and found no significant differences (P > 0.05). In conclusion, these results indicated that Gel/AEAA-Exos has excellent biological compatibility and is suitable for clinical application.

2.11. The Antihepatic Fibrosis Effects of the Hydrogel/Exosome Delivery System. *2.11.1. Assessment of HE, Masson, Sirius Red Stains and RT-PCR.* Figure 7A shows the process of establishing an hepatic fibrosis model and antifibrosis using C57BL/6J mice as research objects. After anesthesia, the livers of the mice in the different groups (Normal, Model, Gel, Gel/Exos, Gel/AEAA-Exos) were removed. Macroscopic observation revealed that the livers of the Model and Gel groups had obvious fibrotic scar formation. The liver surfaces in the Normal group appeared relatively smooth with no noticeable scar formation, whereas no significant difference was observed between the Gel/Exos and Gel/AEAA-Exos groups. HE staining was performed on the livers, and significant inflammatory cell infiltration was observed in both the Model and Gel groups, with no notable differences between them. The inflammatory cell count was markedly lower in both the Gel/AEAA-Exos and Gel/Exos groups than in the Model and Gel groups, and significantly lower in the Gel/AEAA-Exos group than in the Gel/Exos group (Figures 7B and 8D). Masson's staining indicated pronounced hepatic fibrosis in the Model and Gel groups, with collagen fibers arranged in circular patterns (blue cords), creating pseudolobules that linked various portal areas and reached the central vein area. In the Gel/Exos and Gel/AEAA-Exos groups, the structure of these pseudolobules formed by liver fibrosis was less obvious than that in the Model and Gel groups, and even disappeared. Quantitative analysis of the fibrotic tissue showed that therapeutic exosome administration (both Exos and AEAA-Exos formulations) significantly attenuated extracellular matrix remodeling, with lower fibrotic lesions than observed in the Model and Gel-only groups. Moreover, the Gel/Exos group demonstrated a significantly higher degree of fibrosis than did the Gel/AEAA-Exos group (P < 0.001) (Figure 7E). In addition, collagen fiber distribution patterns characterized by sirius red staining closely paralleled those of Masson's staining. The RT-PCR analysis showed AEAA-modified exosomes released by hydrogel can significantly reduce the gene expression levels of α-SMA, Col1a1 and Col3a1 compared with the non-AEAA modified exosomes (P < 0.01). These experimental results confirmed that compared to the nonvectorized exosome group, the hydrogel/AEAA-Exos system significantly alleviated hepatic fibrosis.

2.11.2. Immunohistochemical Analysis. Emerging evidence suggests that the extracellular matrix deposition of PColla III is a key driver of fibrotic liver progression.[63] Furthermore, the degradation of accumulated collagen is predominantly mediated by matrix metalloproteinases (MMPs), which contribute significantly to the pathogenesis of hepatic fibrosis.[64] Therefore, we performed immunohistochemical experiments on hepatic tissues after different treatments using MMP9 and PColla III as indicators to evaluate the effects of gel/AEAA-Exos on hepatic fibrosis. We observed that PColla III was brown in hepatic tissue, and there was an obvious high expression of PColla III in the Model and Gel groups, whereas PColla III expression was relatively low in the Gel/Exos and Gel/AEAA-Exos groups. Moreover, Gel/AEAA-Exos demonstrated superior efficacy in suppressing collagen III deposition, as evidenced by its significantly lower hepatic PColla III expression than that in the Gel/Exos group (Figures 7B and 8F). Figure 7C shows the immunohistochemical stain for MMP9 in the livers of the different groups. MMP9 was less distributed in the Model and Gel groups and more distributed in the Gel/Exos and Gel/AEAA-Exos groups. Comparative quantification demonstrated notably elevated MMP9 expression in the Gel/AEAA-Exos group relative to that in the Model group (Figure 7G). In conclusion, these results confirmed that Gel/AEAA-Exos had a significant

https://doi.org/10.1021/acsnano.5c06003
ACS Nano 2025, 19, 34575−34595

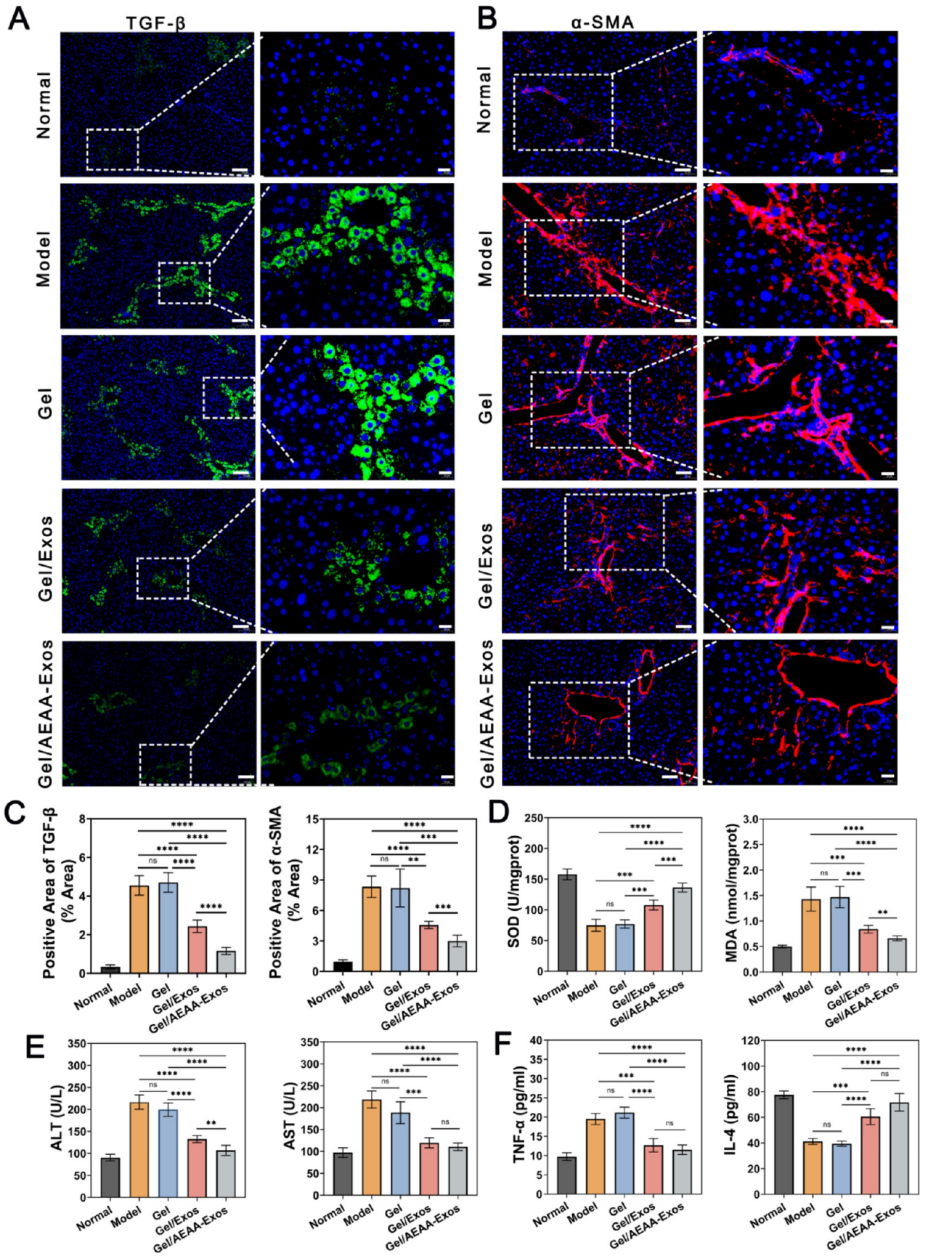

Figure 8. Immunofluorescence assessment and serological assessment of in vivo antihepatic fibrosis of the hydrogel/exosome system. (A, B) The antifibrosis effect of gel/AEAA-Exos system was evaluated by TGF-β and α-SMA, respectively (scale bar of A: low: 100 μm, high: 20 μm, scale bar of B: low: 50 μm, high: 20 μm). (C) Quantification analysis of the TGF-β-positive expression area, the α-SMA-positive expression area. (D) Oxidative stress levels (SOD and MDA) evaluated by Elisa. (E) Serum ALT and AST levels evaluated by Elisa. (F) Inflammatory

https://doi.org/10.1021/acsnano.5c06003
ACS Nano 2025, 19, 34575−34595

Figure 8. continued

levels (TNF-α and IL-4) evaluated by Elisa. Data are presented as means ± SD (n = 5). **P < 0.01, ***P < 0.001, ****P < 0.0001, P > 0.05 (ns, not significant).

antifibrotic effect. Soura et al. confirmed that MMP9 expression increases with the regression of liver fibrosis, suggesting that MMPs play an important role in the regression of fibrosis.[65]

2.11.3. Tissue Immunofluorescence Analysis. Transforming growth factor-β (TGF-β) functions as a potent activator triggering the phenotypic transition of quiescent HSCs into myofibroblasts and a variety of pro-fibrotic factors to promote the occurrence of hepatic fibrosis.[60] Additionally, α-SMA deposition constitutes a hallmark of fibrogenic activation during hepatic fibrogenesis.[60,65] Therefore, we used TGF-β and α-SMA to investigate the lesions of hepatic fibrosis. As shown in Figure 8A,C, the green fluorescence signal represents TGF-β, and comparative assessment revealed markedly elevated TGF-β expression in both the Model and Gel groups, surpassing levels detected in the Gel/Exos and Gel/AEAA-Exos therapeutic groups. Moreover, the TGF-β expression level in the Gel/AEAA-Exos group was markedly reduced compared to that in the Gel/Exos group (P < 0.0001). As shown in Figure 8B,C, immunofluorescence quantification revealed significantly higher expression of α-SMA (red fluorescence) in both the Model and Gel groups than in the Gel/Exos and Gel/AEAA-Exos groups. Moreover, compared with that in the Gel/Exos group, the α-SMA expression level substantially decreased in the Gel/AEAA-Exos group (P < 0.0001). In an hepatic fibrosis model, Li et al.[11] found that hucMSC-derived exosomes attenuated hepatic fibrogenesis through TGF-β1/Smad3 axis inhibition, suppressing HSC transdifferentiation into collagen-producing myofibroblasts. In this study, the Gel/AEAA-Exos formulation demonstrated dual antifibrotic efficacy, reducing the protein abundance of TGF-β and α-SMA versus that of comparator groups, suggesting that AEAA-vectorized exosomes have a better targeting ability against aHSCs in liver tissue and that the Gel/AEAA-Exos system can inhibit the generation of collagen fibers, delay the development of hepatic fibrosis, and effectively alleviate hepatic fibrosis.

2.11.4. Oxidative Stress Analysis. Substantial experimental data have established that oxidative stress is a critical contributor to the pathogenesis of hepatic fibrosis.[66−69] ROS produced by injured liver cells can activate HSCs and induce them to increase collagen production. Therefore, oxidative stress acts as a critical mediator in the pathogenesis of hepatic fibrosis, and antioxidants can prevent these effects. Superoxide dismutase (SOD) and malondialdehyde (MDA) serve as pivotal biomarkers of cellular redox homeostasis, with well-characterized roles in oxidative stress responses and free-radical metabolism. Moreover, in chronic hepatic lesions, antioxidant enzymes such as SOD are downregulated, making the liver sensitive to damage caused by superoxides.[70] The redox landscape during fibrotic regression shows significant MDA depletion, reflecting attenuated lipid peroxidation cascades.[71] In this study, SOD and MDA indices were used to evaluate the effects of Gel/AEAA-Exos on oxidative stress in hepatic fibrosis. As shown in Figure 8D, quantitative analysis demonstrated markedly elevated SOD levels in the Gel/AEAA-Exos group compared with those in the Gel/Exos group, with values approaching the physiological ranges observed in control specimens. Additionally, biochemical profiling revealed substantial attenuation of MDA levels in the Gel/AEAA-Exos group, demonstrating lower fibrotic deposition compared to those in the Gel/Exos group (P < 0.01). These findings demonstrated the therapeutic efficacy of Gel/AEAA-Exos in attenuating fibrotic redox imbalance with concomitant regression of hepatic collagen deposition, thereby confirming that oxidative stress is a pathogenic driver of liver fibrogenesis.

2.11.5. Serological Analysis. The pathophysiological interplay between liver fibrosis and inflammatory processes drives measurable alterations in serum hepatic enzymes and circulating proinflammatory cytokines. For example, when liver function is impaired, the ALT and AST levels in the blood rise.[72] In addition, this interplay was found to upregulate proinflammatory mediators, including TNF-α,[56] while suppressing anti-inflammatory cytokine production, notably that of IL-4.[73] Therefore, these biomarkers were used to assess the hydrogel's antifibrotic efficacy in attenuating pathological collagen deposition during hepatic fibrogenesis. Figure 8E revealed that ALT and AST levels in the Model and Gel groups markedly increased compared with those in the Normal group, while serum transaminase profiling revealed marked reductions in ALT/AST levels across the therapeutic groups (Gel/Exos and Gel/AEAA-Exos) compared to those in the Model group. Notably, the ALT levels in the Gel/AEAA-Exos group were significantly lower than those in the Gel/Exos group. However, the AST levels in the Gel/AEAA-Exos group were not significantly different from those in the Gel/Exos group. As shown in Figure 8F, quantitative analysis revealed attenuated TNF-α expression in both the Gel/Exos and Gel/AEAA-Exos groups compared to that in the Model group, concomitant with elevated IL-4 levels. Notably, no significant differences in cytokine profiles were observed between the two therapeutic groups. In conclusion, the serological results showed that hydrogel-mediated AEAA-exosome delivery attenuated hepatocyte necrosis biomarkers, which was beneficial in reversing hepatic fibrosis.

2.12. Antifibrosis Mechanism of Gel/AEAA-Exos System. The antifibrotic mechanism of Gel/AEAA-Exos in liver models was analyzed by transcriptomic RNA-seq (Figure 9). A total of 1398 differentially expressed genes (DEGs) were identified in treated groups and disease models, with 28 genes shared across all groups (Figure 9A). Pathological models showed 152 upregulated and 58 downregulated genes compared with control (Figure 9B). Gel/AEAA-Exos treatment induced marked expression changes were observed with 1355 genes upregulated and 443 genes downregulated compared with untreated models (Figure 9C).

KEGG pathway analysis revealed distinct molecular associations between experimental groups (Figure 9D,E). Differentially expressed genes predominantly linked to oxidative stress-related pathways (MAPK, PPAR, TGF-β) and cellular adhesion mechanisms were observed in model cohorts (Figure 9D), highlighting the pivotal role of oxidative stress in hepatic fibrosis progression. Conversely, the Gel/AEAA-Exos group exhibited gene enrichment in pathways governing oxidative stress, fibrosis resolution, and inflamma-

https://doi.org/10.1021/acsnano.5c06003
ACS Nano 2025, 19, 34575−34595

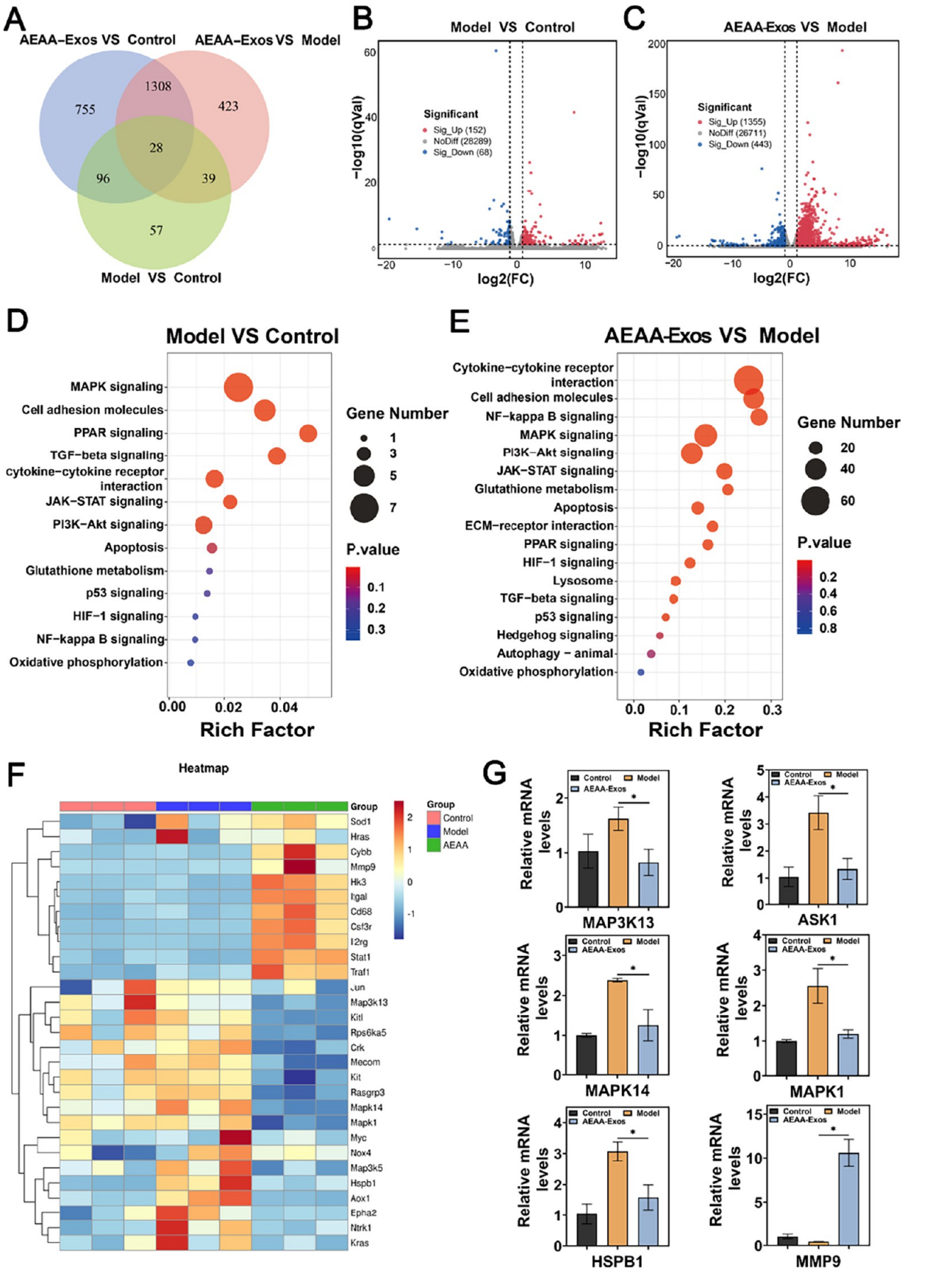

Figure 9. Transcriptome RNA sequencing to evaluate the mechanism of Gel/AEAA-Exos delivery system in alleviating liver fibrosis. (A) Venn diagram of different groups of differential genes. (B, C) Volcanic maps of differential genes in model group and Gel/AEAA-Exos group. (D, E) KEGG Scatter Plot analysis of differential gene-related pathways in the model group and Gel/AEAA-Exos group. (F) Heat map

https://doi.org/10.1021/acsnano.5c06003
ACS Nano 2025, 19, 34575−34595

Figure 9. continued

analysis of genes related to antifibrosis pathways in this study. (G) The gene expression levels of MAP3K13, ASK1, MAPK14, MAPK1, HSPB1 and MMP9 were evaluated by RT-PCR. Data are presented as means ± SD (n = 3). *P < 0.05, **P < 0.01, ***P < 0.001.

tion, including MAPK pathway, NF-κB signaling, cytokine-cytokine receptor interactions, glutathione metabolism, and JAK-STAT cascades (Figure 9E). These findings suggested that the Gel/AEAA-Exos system mitigates fibrogenesis by coordinating oxidative stress modulation, collagen deposition, and inflammatory responses in hepatic tissues. It can be also observed that among all the pathways, the MAPK pathway showed significant expression levels throughout the occurrence and reversal of liver fibrosis (Figure 9D,E). This suggested that the MAPK pathway plays a crucial role in the treatment of liver fibrosis with Gel/AEAA-Exos.

To elucidate the molecular mechanisms of the Gel/AEAA-Exos system, targeted gene analysis was performed with a focus on oxidative stress regulation and fibrotic pathways. The RNA sequencing data indicated that the MAPK/P38 (MAPK14) pathway and the MAPK/ERK (MAPK1) pathway were significantly downregulated, with the upstream genes MAP3K13 and ASK1 showing significant downregulation, and the downstream gene HSPB1 also showing significant downregulation, while MMP9 was significantly upregulated (Figure 9F). Therefore, in this study, the gene expression levels of MAP3K13, ASK1, MAPK/P38, MAPK/ERK, HSPB1, and MMP9 were evaluated by RT-PCR. The results suggested that compared with the model group, the expression levels of MAP3K13, ASK1, MAPK/P38, MAPK/ERK, and HSPB1 in the treatment group were significantly lower, while MMP9 was significantly higher (Figure 9G). The expression of pro-fibrotic genes (such as α-SMA, Col1a1 and Co13a1) was significantly downregulated (Figure S18, P < 0.01). The changes in key pathway node genes are highly consistent with the RNA-seq results. These data provide direct evidence for the mechanism at the transcriptional level. And relevant literature,[74−76] reports indicate that the MAPK pathway shows a downward trend after alleviating liver fibrosis and plays an important role in the reversal of liver fibrosis by regulating oxidative stress. Therefore, the results of RT-PCR, combing with the RNA sequencing, inflammatory indicators TNF-α detected by Elisa and the oxidative stress indicators MDA and SOD (Figure 8), suggested that the Gel/AEAA-Exos system can effectively inhibit the activation of hepatic stellate cells by suppressing the MAPK pathway, thereby reversing or delaying the process of liver fibrosis.

3. CONCLUSIONS

In summary, we designed a powerful hydrogel/exosome delivery platform to sustainably release exosomes targeting aHSCs by local intraperitoneal injection and modification of exosomes and verified its therapeutic effect in a mouse model of CCl_4/olive oil-induced hepatic fibrosis. Moreover, RNA sequencing showed that the Gel/AEAA-Exos system based on CMC-OD/TA-Fe gel and AEAA could slow down the occurrence and formation of liver fibrosis by regulating oxidative stress, collagen deposition and inflammatory response in liver tissue. The platform may represent a new healthy, safe, and efficient strategy for the treatment and prevention of hepatic fibrosis and even hepatic cirrhosis. This work also suggests the application potential of the Gel/AEAA-Exos delivery system for chronic liver injury and end-stage liver disease.

4. METHODS

4.1. Materials. Necessary materials, reagents and equipment required for the experiments are described in the Supporting Information.

4.2. Preparation and Characterization of Materials. *4.2.1. Preparation of Oxidized Dextran (OD).* Oxidation of dextran with sodium periodate ($NaIO_4$) successfully generated the oxidized derivative OD. The OD was evaluated using ^{1}H NMR and FTIR. This method was based on previous studies and was slightly modified to obtain OD.[43] The OD oxidation degree was determined by the hydroxylamine hydrochloride titration method.

4.2.2. Extraction and Characterization of Exosomes. Wharton's jelly derived MSCs were obtained through standardized tissue dissociation procedures from umbilical cord specimens separated from healthy young pregnant women aged 30, and the extracted stem cells were identified by morphology and flow cytometry. The study was conducted with the consent of the participants' families, who signed informed consent forms. Exosomes derived from umbilical cord MSCs were characterized by TEM, NTA, and Western blotting.

4.2.3. Synthesis and Morphological Evaluation of Hydrogels. CMC-OD/TA-Fe/Exos hydrogels system were synthesized by cross-linking CMC and OD (containing exosomes and TA-Fe). The synthesized hydrogels were evaluated using SEM, elemental energy spectrometry (EDS), and FTIR.

4.3. Evaluation of Injectability and Self-Healing. First, the gelling time of the hydrogels was determined via the inverted vial technique. The injectability and self-healing properties of the CMC-OD/TA-Fe hydrogel were evaluated as described in the Supporting Information.

4.4. Viscoelasticity and Adhesion Properties. The viscoelasticity and adhesion properties of the CMC-OD/TA-Fe hydrogel were evaluated using bending, pigskin, and organ adhesion tests, as described in the Supporting Information.

4.5. Degradation and Swelling Properties of Hydrogels. The in vitro degradation and swelling properties of the CMC-OD/TA-Fe hydrogel were evaluated by immersion tests, as described in Supporting Information.

4.6. Rheological Properties of Hydrogels. The rheological properties of the CMC-OD-TA-Fe hydrogel were characterized through oscillatory time sweep measurements, with particular focus on their storage (G') and loss (G'') moduli. The critical strain point was evaluated using an oscillatory amplitude sweep experiment. The self-healing properties of the hydrogels were evaluated using dynamic stepwise strain experiments.

4.7. State of Exosomes Encapsulated in Hydrogels and Sustained-Release Characteristics. Exosomes labeled with PKH-26 and coated in hydrogel were observed using confocal microscopy to evaluate their states. The total amount of exosomes released by hydrogels over time was quantitatively analyzed using a microplate reader to evaluate the sustained-release characteristics.

4.8. Preparation of AEAA-Exos. DSPE-PEG-AEAA was added to the exosome mixture and mixed to obtain AEAA-Exos as described in the Supporting Information.

4.9. Biocompatibility Evaluation of Hydrogels. The biocompatibility of the CMC-OD/TA-Fe/AEAA-Exos system was assessed using cell viability, adhesion, toxicity, hemolysis, and coagulation tests.

4.10. Evaluation of Targeting of AEAA-Exos In Vitro. The ability of AEAA-vectorized exosomes to target aHSCs was evaluated by analyzing the number of exosomes taken up in aHSCs, AML-12 cells and blocked aHSCs with AEAA.

https://doi.org/10.1021/acsnano.5c06003
ACS Nano 2025, 19, 34575−34595

4.11. Evaluation of Antioxidant and Antifibrotic Properties of AEAA-Exos In Vitro. The in vitro antioxidant activity of AEAA-modified exosomes was evaluated using a DCFH-DA fluorescent probe. The in vitro antifibrotic activity of AEAA-modified exosomes was evaluated by α-SMA and Col1a I.

4.12. Evaluation of Targeting of AEAA-Exos In Vivo. The in vivo targeting ability of the hydrogel/exosome delivery system was evaluated using small-animal imaging and tissue immunofluorescence experiments.

4.13. Animal Research. The in vivo biosafety and antifibrotic effects of hydrogel/AEAA-Exos system were assessed in C57BL/6J mouse hepatic fibrosis models. Biosafety used HE staining and serology. Fibrosis was evaluated via HE, Masson's trichrome, sirius red staining, RT-PCR. The system's therapeutic impact was further analyzed using immunohistochemistry, immunofluorescence, and ELISA (for oxidative stress modulation). Serum liver function and inflammation indices were measured. Detailed experimental groupings and procedures are in Supporting Information.

4.14. Statistical Analysis. GraphPad Prism 10.1 (GraphPad Software, La Jolla, CA) was used to analyze the experimental data in this study. Parametric tests were performed with Student's t test assessing pairwise comparisons and ANOVA applied for multigroup analyses. ns means no significant difference, while $^{*}P < 0.05$, $^{**}P < 0.01$, $^{***}P < 0.001$, and $^{****}P < 0.0001$ illustrate statistically significant differences.

ASSOCIATED CONTENT

Supporting Information

The Supporting Information is available free of charge at https://pubs.acs.org/doi/10.1021/acsnano.5c06003.

Extraction and identification of human umbilical cord mesenchymal stem cells; the NTA for isolated exosomes; the gelation time assessment for the prepared hydrogel; the adhesion properties for the prepared hydrogel to porcine skin; the adhesion properties for the prepared hydrogel to organs; state analysis of exosomes encapsulated in hydrogel; biocompatibility of different hydrogel extracts to BRL-3A cells; evaluation of the in vitro targeting properties of AEAA-modified exosomes; evaluation of in vitro targeting properties for AEAA-modified exosomes by flow cytometry; flow cytometric assessment for the blocking experiment mediated by Sigma receptors on the surface of aHSCs; evaluation of in vitro anti-ROS properties for AEAA-modified exosomes by flow cytometry; evaluation of in vitro antifibrosis properties for AEAA-modified exosomes by RT-PCR; organ histological assessment for liver fibrosis model; evaluation of exosomes distribution in isolated organs; the metabolic status assessment of AEAA-modified exosomes in the gastrointestinal system by small animal imaging and tissue immunofluorescence; the safety assessment of the hydrogel/exosome system on brain tissue through HE staining; the state or degeneration assessment at different time points for the hydrogel/exosome system implanted in C57BL/6J mice; evaluation of in vivo antifibrosis properties for Gel/AEAA-Exos system by RT-PCR; the characterization of the combination of AEAA and exosomes; evaluation of intestinal adhesion and obstruction events induced by the hydrogel/AEAA-Exos system; characterization of different nanoparticles; criterion of cytotoxicity assessment; related data on exosome yield and purity (PDF)

AUTHOR INFORMATION

Corresponding Authors

Jia Yao − *First Clinical Medical College, Lanzhou University, Lanzhou 730000, China; Key Laboratory of Biotherapy and Regenerative Medicine, First Hospital of Lanzhou University, Lanzhou University, Lanzhou 730000, China;* orcid.org/0000-0002-0811-8287; Email: yaoj06@lzu.edu.cn

Xun Li − *First Clinical Medical College, Lanzhou University, Lanzhou 730000, China; Key Laboratory of Biotherapy and Regenerative Medicine, First Hospital of Lanzhou University, Lanzhou University, Lanzhou 730000, China; General Surgery Department, First Hospital of Lanzhou University, Lanzhou University, Lanzhou 730000, China; Hepatopancreatobiliary Surgery Institute of Gansu Province, Lanzhou 730000, China; Clinical Research Center for General Surgery of Gansu Province, Lanzhou 730000, China; Gansu Provincial Engineering Research Center for Translational Liver Repair and Regenerative Medicine, Lanzhou 730000, China; Cancer Prevention and Treatment Center, Lanzhou University School of Medicine, Lanzhou 730000, China;* orcid.org/0000-0001-6862-7692; Email: lxdr21@126.com

Authors

Zongbin Sun − *First Clinical Medical College, Lanzhou University, Lanzhou 730000, China*

Qiuxia Zheng − *First Clinical Medical College, Lanzhou University, Lanzhou 730000, China*

Yue Zhang − *First Clinical Medical College, Lanzhou University, Lanzhou 730000, China*

Chongyang Bai − *First Clinical Medical College, Lanzhou University, Lanzhou 730000, China*

Fanghong Wang − *First Clinical Medical College, Lanzhou University, Lanzhou 730000, China; Key Laboratory of Biotherapy and Regenerative Medicine, First Hospital of Lanzhou University, Lanzhou University, Lanzhou 730000, China; General Surgery Department, First Hospital of Lanzhou University, Lanzhou University, Lanzhou 730000, China*

Ping Yang − *First Clinical Medical College, Lanzhou University, Lanzhou 730000, China*

Dan Zhu − *First Clinical Medical College, Lanzhou University, Lanzhou 730000, China; Key Laboratory of Biotherapy and Regenerative Medicine, First Hospital of Lanzhou University, Lanzhou University, Lanzhou 730000, China; General Surgery Department, First Hospital of Lanzhou University, Lanzhou University, Lanzhou 730000, China*

Xiaoyuan Liu − *First Clinical Medical College, Lanzhou University, Lanzhou 730000, China*

Shang Li − *First Clinical Medical College, Lanzhou University, Lanzhou 730000, China*

Desheng Liu − *State Key Laboratory of Solid Lubrication, Lanzhou Institute of Chemical Physics, Chinese Academy of Sciences, Lanzhou 730000, China;* orcid.org/0009-0009-0476-7157

Rui Li − *First Clinical Medical College, Lanzhou University, Lanzhou 730000, China*

Liu He − *Gansu Provincial Engineering Research Center for Translational Liver Repair and Regenerative Medicine, Lanzhou 730000, China*

Complete contact information is available at: https://pubs.acs.org/10.1021/acsnano.5c06003

https://doi.org/10.1021/acsnano.5c06003
ACS Nano 2025, 19, 34575−34595

Notes

The authors declare no competing financial interest.

ACKNOWLEDGMENTS

This work was supported by the National Natural Science Foundation of China regional project (82060119), Gansu Provincial General Surgery Clinical Medical Research Center (20JR10FA661). Gansu Province Traditional Chinese Medicine Industry Innovation Consortium Project (22ZD6FA021-4) and the Gansu Province Science and Technology Plan Project (23YFFA0034). International cooperation field of major scientific and technological projects (23ZDWA003) -- China and Germany jointly develop a new generation of stem cell therapy technology for hepatic fibrosis/cirrhosis. Gansu Province Graduate Innovation Funding Project (2025CXZX-019).

REFERENCES

(1) Dhar, D.; Baglieri, J.; Kisseleva, T.; Brenner, D. A. Mechanisms of liver fibrosis and its role in liver cancer. *Exp. Biol. Med.* **2020**, *245*, 96−108.
(2) Parola, M.; Pinzani, M. Liver fibrosis: Pathophysiology, pathogenetic targets and clinical issues. *Mol. Aspects Med.* **2019**, *65*, 37−55.
(3) Caligiuri, A.; Gentilini, A.; Pastore, M.; Gitto, S.; Marra, F. Cellular and Molecular Mechanisms Underlying Liver Fibrosis Regression. *Cells* **2021**, *10*, No. 2759.
(4) Llovet, J. M.; Kelley, R. K.; Villanueva, A.; Singal, A. G.; Pikarsky, E.; Roayaie, S.; Lencioni, R.; Koike, K.; Zucman-Rossi, J.; Finn, R. S. Hepatocellular carcinoma. *Nat. Rev. Dis Primers* **2021**, *7*, No. 6.
(5) Gines, P.; Krag, A.; Abraldes, J. G.; Sola, E.; Fabrellas, N.; Kamath, P. S. Liver cirrhosis. *Lancet* **2021**, *398*, 1359−1376.
(6) Higashi, T.; Friedman, S. L.; Hoshida, Y. Hepatic stellate cells as key target in liver fibrosis. *Adv. Drug Delivery Rev.* **2017**, *121*, 27−42.
(7) Rani, S.; Ryan, A. E.; Griffin, M. D.; Ritter, T. Mesenchymal Stem Cell-derived Extracellular Vesicles: Toward Cell-free Therapeutic Applications. *Mol. Ther.* **2015**, *23*, 812−823.
(8) Tsiapalis, D.; O'Driscoll, L. Mesenchymal Stem Cell Derived Extracellular Vesicles for Tissue Engineering and Regenerative Medicine Applications. *Cells* **2020**, *9*, No. 991.
(9) Yin, F.; Wang, W.-Y.; Jiang, W.-H. Human umbilical cord mesenchymal stem cells ameliorate liver fibrosis in vitro and in vivo: From biological characteristics to therapeutic mechanisms. *World J. Stem Cells* **2019**, *11*, 445−564.
(10) He, Y.; Guo, X.; Lan, T.; Xia, J.; Wang, J.; Li, B.; Peng, C.; Chen, Y.; Hu, X.; Meng, Z. Human umbilical cord-derived mesenchymal stem cells improve the function of liver in rats with acute-on-chronic liver failure via downregulating Notch and Stat1/Stat3 signaling. *Stem Cell Res. Ther.* **2021**, *12*, No. 396.
(11) Li, T.; Yan, Y.; Wang, B.; Qian, H.; Zhang, X.; Shen, L.; Wang, M.; Zhou, Y.; Zhu, W.; Li, W.; et al. Exosomes derived from human umbilical cord mesenchymal stem cells alleviate liver fibrosis. *Stem Cells Dev.* **2013**, *22*, 845−854.
(12) Kang, Y.; Song, Y.; Luo, Y.; Song, J.; Li, C.; Yang, S.; Guo, J.; Yu, J.; Zhang, X. Exosomes derived from human umbilical cord mesenchymal stem cells ameliorate experimental non-alcoholic steatohepatitis via Nrf2/NQO-1 pathway. *Free Radical Biol. Med.* **2022**, *192*, 25−36.
(13) Zhang, J.; Fu, B.; Li, M.; Mi, S. Secretome of Activated Fibroblasts Induced by Exosomes for the Discovery of Biomarkers in Non-Small Cell Lung Cancer. *Small* **2021**, *17*, No. e2004750.
(14) Bavisotto, C. C.; Cappello, F.; Macario, A. J. L.; de Macario, E. C.; Logozzi, M.; Fais, S.; Campanella, C. Exosomal HSP60: a potentially useful biomarker for diagnosis, assessing prognosis, and monitoring response to treatment. *Expert Rev. Mol. Diagn.* **2017**, *17*, 815−822.
(15) Wu, H.; Fu, M.; Liu, J.; Chong, W.; Fang, Z.; Du, F.; Liu, Y.; Shang, L.; Li, L. The role and application of small extracellular vesicles in gastric cancer. *Mol. Cancer* **2021**, *20*, No. 71.
(16) Baek, S.; Jeon, M.; Jung, H. N.; Lee, W.; Hwang, J.-E.; Lee, J. S.; Choi, Y.; Im, H.-J. M1Macrophage-Derived Exosome-Mimetic Nanovesicles with an Enhanced Cancer Targeting Ability. *ACS Appl. Bio Mater.* **2022**, *5*, 2862−2869.
(17) Cao, H.; Duan, L.; Zhang, Y.; Cao, J.; Zhang, K. Current hydrogel advances in physicochemical and biological response-driven biomedical application diversity. *Signal Transduction Targeted Ther.* **2021**, *6*, No. 426.
(18) Li, L.; Zhang, Y.; Mu, J.; Chen, J.; Zhang, C.; Cao, H.; Gao, J. Transplantation of Human Mesenchymal Stem-Cell-Derived Exosomes Immobilized in an Adhesive Hydrogel for Effective Treatment of Spinal Cord Injury. *Nano Lett.* **2020**, *20*, 4298−4305.
(19) Abourehab, M. A. S.; Pramanik, S.; Abdelgawad, M. A.; Abualsoud, B. M.; Kadi, A.; Ansari, M. J.; Deepak, A. Recent Advances of Chitosan Formulations in Biomedical Applications. *Int. J. Mol. Sci.* **2022**, *23*, No. 10975.
(20) El-Hack, M. E. A.; El-Saadony, M. T.; Shafi, M. E.; Zabermawi, N. M.; Arif, M.; Batiha, G. E.; Khafaga, A. F.; El-Hakim, Y. M. A.; Al-Sagheer, A. A. RETRACTED: Antimicrobial and antioxidant properties of chitosan and its derivatives and their applications: A review. *Int. J. Biol. Macromol.* **2020**, *164*, 2726−2744.
(21) Zou, C.-Y.; Lei, X.-X.; Hu, J.-J.; Jiang, Y.-L.; Li, Q.-J.; Song, Y.-T.; Zhang, Q.-Y.; Ling, J. L.; Xie, H.-Q. Multi-crosslinking hydrogels with robust bio-adhesion and pro-coagulant activity for first-aid hemostasis and infected wound healing. *Bioact. Mater.* **2022**, *16*, 388−402.
(22) Zhu, Z.; Zhang, K.; Xian, Y.; He, G.; Pan, Z.; Wang, H.; Zhang, C.; Wu, D. A Choline Phosphoryl-conjugated Chitosan/Oxidized Dextran Injectable Self-Healing Hydrogel for Improved Hemostatic Efficacy. *Biomacromolecules* **2023**, *24*, 690−703.
(23) Wang, H.; Liu, D.; Zhang, L.; Gao, X.; Nie, Y.; Liu, Y.; Jia, Y.; Yin, M.; Qiao, X. Label-Free Small Extracellular Vesicles Capturing Strategy for Lung Cancer Diagnosis and Typing Based on a Natural Polyphenol-Metal Three-Dimensional Network. *Anal. Chem.* **2022**, *94*, 16103−16112.
(24) Fan, H.; Wang, J.; Zhang, Q.; Jin, Z. Tannic Acid-Based Multifunctional Hydrogels with Facile Adjustable Adhesion and Cohesion Contributed by Polyphenol Supramolecular Chemistry. *ACS Omega* **2017**, *2*, 6668−6676.
(25) Sun, J.; Chen, T.; Zhao, B.; Fan, W.; Shen, Y.; Wei, H.; Zhang, M.; Zheng, W.; Peng, J.; Wang, J.; et al. Acceleration of Oral Wound Healing under Diabetes Mellitus Conditions Using Bioadhesive Hydrogel. *ACS Appl. Mater. Interfaces* **2023**, *15*, 416−431.
(26) Yu, Y.; Li, P.; Zhu, C.; Ning, N.; Zhang, S.; Vancso, G. J. Multifunctional and Recyclable Photothermally Responsive Cryogels as Efficient Platforms for Wound Healing. *Adv. Funct. Mater.* **2019**, *29*, No. 1904402.
(27) Lin, X.; Zhang, H.; Li, S.; Huang, L.; Zhang, R.; Zhang, L.; Yu, A.; Duan, B. Polyphenol-driving assembly for constructing chitin-polyphenol-metal hydrogel as wound dressing. *Carbohydr. Polym.* **2022**, *290*, No. 119444.
(28) Zhuo, Z.; Wang, J.; Luo, Y.; Zeng, R.; Zhang, C.; Zhou, W.; Guo, K.; Wu, H.; Sha, W.; Chen, H. Targeted extracellular vesicle delivery systems employing superparamagnetic iron oxide nanoparticles. *Acta Biomater.* **2021**, *134*, 13−31.
(29) Hu, M.; Wang, Y.; Xu, L.; An, S.; Tang, Y.; Zhou, X.; Li, J.; Liu, R.; Huang, L. Relaxin gene delivery mitigates liver metastasis and synergizes with check point therapy. *Nat. Commun.* **2019**, *10*, No. 2993.
(30) Jiang, M.; He, K.; Qiu, T.; Sun, J.; Liu, Q.; Zhang, X.; Zheng, H. Tumor-targeted delivery of silibinin and IPI-549 synergistically inhibit breast cancer by remodeling the microenvironment. *Int. J. Pharm.* **2020**, *581*, No. 119239.
(31) Vu, N. B.; Nguyen, H. T.; Palumbo, R.; Pellicano, R.; Fagoonee, S.; Pham, P. V. Stem cell-derived exosomes for wound

https://doi.org/10.1021/acsnano.5c06003
ACS Nano 2025, 19, 34575−34595

healing: current status and promising directions. *Minerva Med.* **2020**, *112*, 384−400.
(32) Zhang, Z.; Shang, J.; Yang, Q.; Dai, Z.; Liang, Y.; Lai, C.; Feng, T.; Zhong, D.; Zou, H.; Sun, L.; et al. Exosomes derived from human adipose mesenchymal stem cells ameliorate hepatic fibrosis by inhibiting PI3K/Akt/mTOR pathway and remodeling choline metabolism. *J. Nanobiotechnol.* **2023**, *21*, No. 29.
(33) Zou, J.; Yang, W.; Cui, W.; Li, C.; Ma, C.; Ji, X.; Hong, J.; Qu, Z.; Chen, J.; Liu, A.; Wu, H. Therapeutic potential and mechanisms of mesenchymal stem cell-derived exosomes as bioactive materials in tendon−bone healing. *J. Nanobiotechnol.* **2023**, *21*, No. 14.
(34) Liu, A.; Liang, X.; Wang, W.; Wang, C.; Song, J.; Guo, J.; Sun, D.; Wang, D.; Song, M.; Qian, J.; Zhang, X. Human umbilical cord mesenchymal stem cells ameliorate colon inflammation via modulation of gut microbiota-SCFAs-immune axis. *Stem Cell Res. Ther.* **2023**, *14*, No. 271.
(35) Yang, K.; Zhou, X.; Li, Z.; Wang, Z.; Luo, Y.; Deng, L.; He, D. Ultrastretchable, Self-Healable, and Tissue-Adhesive Hydrogel Dressings Involving Nanoscale Tannic Acid/Ferric Ion Complexes for Combating Bacterial Infection and Promoting Wound Healing. *ACS Appl. Mater. Interfaces* **2022**, *14*, 43010−43025.
(36) Liu, Q.; Wang, C.; Cheng, M.; Hu, L.; Zhang, Z.; Sun, Q.; Wang, S.; Fan, Y.; Pan, P.; Chen, J. Self-Healing Conductive Hydrogels with Dynamic Dual Network Structure Accelerate Infected Wound Healing via Photothermal Antimicrobial and Regulating Inflammatory Response. *ACS Appl. Mater. Interfaces* **2024**, *16*, 30776−30792.
(37) Van der Meel, R.; Fens, M. H. A. M.; Vader, P.; van Solinge, W. W.; Eniola-Adefeso, O.; Schiffelers, R. M. Extracellular vesicles as drug delivery systems: Lessons from the liposome field. *J. Controlled Release* **2014**, *195*, 72−85.
(38) Gupta, A. D.; Krawczynska, N.; Nelson, E. R. Extracellular Vesicles-The Next Frontier in Endocrinology. *Endocrinology* **2021**, *162*, No. bqab133.
(39) Li, M.; Tang, H.; Geng, X.; Zhou, J.; Mou, S.; Li, C.; Chang, J.; Xu, M.; Wang, C.; Fu, R.; Wang, Y. All-natural hydrogel composed of carboxymethyl chitosan and oxidized dextran for promoting wound healing by immune-microenvironment regulation. *Carbohydr. Polym.* **2024**, *347*, No. 122731.
(40) Cai, G.; Ren, L.; Yu, J.; Jiang, S.; Liu, G.; Wu, S.; Cheng, B.; Li, W.; Xia, J. A Microenvironment-Responsive, Controlled Release Hydrogel Delivering Embelin to Promote Bone Repair of Periodontitis via Anti-Infection and Osteo-Immune Modulation. *Adv. Sci.* **2024**, *11*, No. e2403786.
(41) Guo, C.; Wu, Y.; Li, W.; Wang, Y.; Kong, Q. Development of a Microenvironment-Responsive Hydrogel Promoting Chronically Infected Diabetic Wound Healing through Sequential Hemostatic, Antibacterial, and Angiogenic Activities. *ACS Appl. Mater. Interfaces* **2022**, *14*, 30480−30492.
(42) Zhao, X.; Li, P.; Guo, B.; Ma, P. X. Antibacterial and conductive injectable hydrogels based on quaternized chitosan-graft-polyaniline/oxidized dextran for tissue engineering. *Acta Biomater.* **2015**, *26*, 236−248.
(43) Zhu, Z.; Zhang, K.; Xian, Y.; He, G.; Pan, Z.; Wang, H.; Zhang, C.; Wu, D. A Choline Phosphoryl-Conjugated Chitosan/Oxidized Dextran Injectable Self-Healing Hydrogel for Improved Hemostatic Efficacy. *Biomacromolecules* **2023**, *24*, 690−703.
(44) Yue, Y.; Liu, Y.; Lin, Y.; Guo, F.; Cai, K.; Chen, S.; Zhang, W.; Tang, S. A carboxymethyl chitosan/oxidized hyaluronic acid composite hydrogel dressing loading with stem cell exosome for chronic inflammation wounds healing. *Int. J. Biol. Macromol.* **2024**, *257*, No. 128534.
(45) Chen, Z.; Zhao, J.; Wu, H.; Wang, H.; Lu, X.; Shahbazi, M.-A.; Wang, S. A triple-network carboxymethyl chitosan-based hydrogel for hemostasis of incompressible bleeding on wet wound surfaces. *Carbohydr. Polym.* **2023**, *303*, No. 120434.
(46) Meena, L. K.; Raval, P.; Kedaria, D.; Vasita, R. Study of locust bean gum reinforced cyst-chitosan and oxidized dextran based semi-IPN cryogel dressing for hemostatic application. *Bioact. Mater.* **2018**, *3*, 370−384.
(47) Weng, L.; Alexander, R.; Jean, R.; Chen, W. Non-cytotoxic, in situ gelable hydrogels composed of N-carboxyethyl chitosan and oxidized dextran. *Biomaterials* **2008**, *29*, 3905−3913.
(48) Zhang, X.; Yang, Y.; Yao, J.; Shao, Z.; Chen, X. Strong Collagen Hydrogels by Oxidized Dextran Modification. *ACS Sustainable Chem. Eng.* **2014**, *2*, 1318−1324.
(49) He, Z.; Yuan, W. Adhesive, Stretchable, and Transparent Organohydrogels for Antifreezing, Antidrying, and Sensitive Ionic Skins. *ACS Appl. Mater. Interfaces* **2021**, *13*, 1474−1485.
(50) Liu, X.; Song, X.; Zhang, Z.; Yang, S.; Li, L.; Lin, C.; Chen, M.; Liu, C.; Li, X.; Zhang, Y.; Hu, G. Multifunctional Oxidized Dextran−Metformin as a Tissue-Adhesive Hydrogel to Prevent Postoperative Peritoneal Adhesions in Patients with Metabolic Syndrome. *Adv. Sci.* **2023**, *10*, No. e2303767.
(51) Guo, S.; Ren, Y.; Chang, R.; He, Y.; Zhang, D.; Guan, F.; Yao, M. Injectable Self-Healing Adhesive Chitosan Hydrogel with Antioxidative, Antibacterial, and Hemostatic Activities for Rapid Hemostasis and Skin Wound Healing. *ACS Appl. Mater. Interfaces* **2022**, *14*, 34455−34469.
(52) Ouyang, C.; Yu, H.; Wang, L.; Ni, Z.; Liu, X.; Shen, D.; Yang, J.; Shi, K.; Wang, H. Tough adhesion enhancing strategies for injectable hydrogel adhesives in biomedical applications. *Adv. Colloid Interface Sci.* **2023**, *319*, No. 102982.
(53) Zhang, F.; Zhang, S.; Lin, R.; Cui, S.; Jing, X.; Coseri, S. High mechanical and self-healing carboxymethyl chitosan-hyaluronic acid hybrid hydrogel via multiple dynamic covalent bonds for drug delivery. *Eur. Polym. J.* **2023**, *197*, No. 112342.
(54) Huang, Y.; Mu, L.; Zhao, X.; Han, Y.; Guo, B. Bacterial Growth-Induced Tobramycin Smart Release Self-Healing Hydrogel for Pseudomonas aeruginosa-Infected Burn Wound Healing. *ACS Nano* **2022**, *16*, 13022−13036.
(55) Qu, J.; Zhao, X.; Liang, Y.; Zhang, T.; Ma, P. X.; Guo, B. Antibacterial adhesive injectable hydrogels with rapid self-healing, extensibility and compressibility as wound dressing for joints skin wound healing. *Biomaterials* **2018**, *183*, 185−199.
(56) Yuan, Y.; Shen, S.; Fan, D. A physicochemical double cross-linked multifunctional hydrogel for dynamic burn wound healing: shape adaptability, injectable self-healing property and enhanced adhesion. *Biomaterials* **2021**, *276*, No. 120838.
(57) Williams, D. F. The plasticity of biocompatibility. *Biomaterials* **2023**, *296*, No. 122077.
(58) ISO. Biological Evaluation of Medical Devices − Part 5: Tests for In Vitro Cytotoxicity. 2009.
(59) Lázaro-Ibáñez, E.; Faruqu, F. N.; Saleh, A. F.; Silva, A. M.; Wang, J. T.-W.; Rak, J.; Al-Jamal, K. T.; Dekker, N. Selection of Fluorescent, Bioluminescent, and Radioactive Tracers to Accurately Reflect Extracellular Vesicle Biodistribution in Vivo. *ACS Nano* **2021**, *15*, 3212−3227.
(60) Hernández-Aquino, E.; Quezada-Ramírez, M. A.; Silva-Olivares, A.; Ramos-Tovar, E.; Flores-Beltrán, R. E.; Segovia, J.; Shibayama, M.; Muriel, P. Curcumin downregulates Smad pathways and reduces hepatic stellate cells activation in experimental fibrosis. *Ann. Hepatol.* **2020**, *19*, 497−506.
(61) Hu, M.; Wang, Y.; Liu, Z.; Yu, Z.; Guan, K.; Liu, M.; Wang, M.; Tan, J.; Huang, L. Hepatic macrophages act as a central hub for relaxin-mediated alleviation of liver fibrosis. *Nat. Nanotechnol.* **2021**, *16*, 466−477.
(62) Zhang, C.; Teng, Y.; Li, F.; Ho, W.; Bai, X.; Xu, X.; Zhang, X.-Q. Nanoparticle-Mediated RNA Therapy Attenuates Nonalcoholic Steatohepatitis and Related Fibrosis by Targeting Activated Hepatic Stellate Cells. *ACS Nano* **2023**, *17*, 14852−14870.
(63) Ryhänen, L.; Stenbäck, F.; Ala-Kokko, L.; Savolainen, E.-R. The effect of malotilate on type III and type IV collagen, laminin and fibronectin metabolism in dimethylnitrosamine-induced liver fibrosis in the rat. *J. Hepatol.* **1996**, *24*, 238−245.

https://doi.org/10.1021/acsnano.5c06003
ACS Nano 2025, 19, 34575−34595

(64) Zhao, P.; Sun, T.; Lyu, C.; Liang, K.; Niu, Y.; Zhang, Y.; Cao, C.; Xiang, C.; Du, Y. Scar-Degrading Endothelial Cells as a Treatment for Advanced Liver Fibrosis. *Adv. Sci.* **2022**, *10*, No. e2203315.
(65) Mardpour, S.; Ghanian, M. H.; Sadeghi-abandansari, H.; Mardpour, S.; Nazari, A.; Shekari, F.; Baharvand, H. Hydrogel-Mediated Sustained Systemic Delivery of Mesenchymal Stem Cell-Derived Extracellular Vesicles Improves Hepatic Regeneration in Chronic Liver Failure. *ACS Appl. Mater. Interfaces* **2019**, *11*, 37421−37433.
(66) Tsuchida, T.; Friedman, S. L. Mechanisms of hepatic stellate cell activation. *Nat. Rev. Gastroenterol. Hepatol.* **2017**, *14*, 397−411.
(67) Ramos-Tovar, E.; Muriel, P. Molecular Mechanisms That Link Oxidative Stress, Inflammation, and Fibrosis in the Liver. *Antioxidants* **2020**, *9*, No. 1279.
(68) Kumar, S.; Duan, Q.; Wu, R.; Harris, E. N.; Su, Q. Pathophysiological communication between hepatocytes and non-parenchymal cells in liver injury from NAFLD to liver fibrosis. *Adv. Drug Delivery Rev.* **2021**, *176*, No. 113869.
(69) Roehlen, N.; Crouchet, E.; Baumert, T. F. Liver Fibrosis: Mechanistic Concepts and Therapeutic Perspectives. *Cells* **2020**, *9*, No. 875.
(70) Ramos-Tovar, E.; Muriel, P. Molecular Mechanisms That Link Oxidative Stress, Inflammation, and Fibrosis in the Liver. *Antioxidants* **2020**, *9*, No. 1279.
(71) Abdelmageed, M. E.; Abdelrahman, R. Canagliflozin attenuates thioacetamide-induced liver injury through modulation of HMGB1/RAGE/TLR4 signaling pathways. *Life Sci.* **2023**, *322*, No. 121654.
(72) Lu, X.; Xuan, W.; Li, J.; Yao, H.; Huang, C.; Li, J. AMPK protects against alcohol-induced liver injury through UQCRC2 to up-regulate mitophagy. *Autophagy* **2021**, *17*, 3622−3643.
(73) Shen, Y.; Shen, X.; Cheng, Y.; Liu, Y. Myricitrin pretreatment ameliorates mouse liver ischemia reperfusion injury. *Int. Immunopharmacol.* **2020**, *89*, No. 107005.
(74) Hao, Y.; Song, S.; Li, T.; Zai, Q.; Ma, N.; Li, Y.; Yang, L.; Xiao, P.; Xu, T.; Ji, L.; et al. Oxidative stress promotes liver fibrosis by modulating the microRNA-144 and SIN3A-p38 pathways in hepatic stellate cells. *Int. J. Biol. Sci.* **2024**, *20*, 2422−2439.
(75) Zhao, W.; Zhang, J.; Guo, Q.; Wang, Q.; Zhao, H.; Xiao, F.; Han, M.; Cao, Y.; Ding, R.; Yang, A.; Xie, W. Fibulin-1 deficiency alleviates liver fibrosis by inhibiting hepatic stellate cell activation via the p38 MAPK pathway. *Cell. Mol. Life Sci.* **2025**, *82*, No. 192.
(76) Liu, X.; Wang, X.; Xu, L.; Fan, J.; Yuan, Q.; Zhang, F.; Liu, J.; Qiu, X.; Li, Y.; Xia, C.; Liu, H. Targeting delivery of a novel TGF-β type I receptor-mimicking peptide to activated hepatic stellate cells for liver fibrosis therapy via inhibiting the TGF-β1/Smad and p38 MAPK signaling pathways. *Eur. J. Pharmacol.* **2024**, *977*, No. 176708.

https://doi.org/10.1021/acsnano.5c06003
ACS Nano 2025, 19, 34575−34595